http://dx.doi.org/10.1039/c2cp41139c

Y.S. Avadhut, J. Weber, E. Hammarberg, C. Feldmann, J. Schmedt auf der Günne. Structural investigation of aluminum doped ZnO nanoparticles by solid-state NMR spectroscopy. *Phys. Chem. Chem. Phys.* **2012**, 14:11610-11625

Structural investigation of Aluminium Doped ZnO Nanoparticles by Solid-State NMR Spectroscopy

Yamini S. Avadhut [a], *Johannes Weber* [a], *Elin Hammarberg* [b], *Claus Feldmann* [b], *Jörn Schmedt auf der Günne** [a]

[a] Ludwig-Maximilians-Universität München, Department Chemie, Butenandtstraße 5-13 (D), D-81377 München, Germany

[b] Institut für Anorganische Chemie, Karlsruhe Institute of Technology (KIT), Engesserstraße 15, D-76131 Karlsruhe, Germany.

RECEIVED DATE (to be automatically inserted after your manuscript is accepted if required according to the journal that you are submitting your paper to)

E-mail: gunnej@cup.uni-muenchen.de

Abstract

The electrical conductivity of aluminium doped zinc oxide (AZO, ZnO:Al) materials depends on doping induced defects and grain structure. This study targets at relating macroscopic electrical conductivity of AZO nano-particles to the their atomic structure which is non-trivial because the derived materials are heavily disordered and heterogeneous in nature. For this purpose we synthesized AZO nanoparticles with different doping levels and narrow size distribution by a microwave assisted polyol method followed by drying and a reductive treatment with forming gas. From these particles electrically conductive, optically transparent films were obtained by spin-coating. Characterization involved energy-dispersive X-ray analysis, wet chemical analysis, X-ray diffraction, electron microscopy and dynamic light scattering which provided a basis for a detailed structural solid-state NMR study. A multinuclear (^{27}Al, ^{13}C, ^{1}H) spectroscopic investigation required a number of 1D MAS NMR and 2D MAS NMR techniques (T_1-measurements, ^{27}Al-MQMAS, ^{27}Al-^{1}H 2D-PRESTOIII heteronuclear correlation spectroscopy), which were corroborated by quantum chemical calculations with an embedded cluster method (EEIM) at DFT level.

From the combined data we conclude that only a small part of the provided Al is incorporated into the ZnO structure by substitution of Zn. The related ^{27}Al NMR signal undergoes a Knight shift when the material is subject to a reductive treatment with forming gas. At higher (formal) doping levels Al forms insulating (Al, H and C containing) side-phases, which cover the surface of the ZnO:Al particles and increase the sheet resistivity of spin-coated material. Moreover calculated ^{27}Al quadrupole coupling constants serve as spectroscopic fingerprint by which previously suggested point-defects can be identified and in their great majority be ruled out.

Keywords: Aluminium doped zinc-oxide, nano, synthesis, non-crystalline, solid-state NMR, transparent conductive oxide, defects, Korringa, Knight shift, DFT, quadrupolar coupling, electric field gradients.

Introduction

Since its first investigations about 30 years ago[1,2] aluminium doped zinc oxide (AZO, ZnO:Al) has gained considerable and continuous interest as a transparent conducting oxide (TCO) for application in various optoelectronic devices,[3] primarily as transparent electrodes in thin film solar cells and flat panel displays.[4] Compared to the other two TCO materials that are frequently used nowadays, namely tin doped indium oxide (ITO, In_2O_3:Sn) and fluorine doped tin oxide (FTO, SnO_2:F), AZO possesses the advantage that it is cheaper and non-toxic. The material prizes gained even more importance in recent years which showed a continuously high demand and increased cost of indium on the one hand[5] and the possibility of energy-efficient fabrication routes of thin films via printing techniques of nanoscaled precursors on the other hand.[6]

The importance of zinc oxide (ZnO) doped with group III elements, especially Al,[5–7] has triggered a huge number of studies on nanoparticles and films, with a focus on optical and electrical properties. Liquid phase preparation of transparent conductive AZO nanocrystals is dominated by sol-gel techniques.[8–12] A number of studies have examined the influence of solvent, temperature,[15] crystallinity,[16] doping concentration[15,17–20] and heating profile[20] on film properties, which slightly differ with respect to the resistivity and optical transparency. Despite the complexity of the material there is a consensus that an optimum doping level exists, which however is difficult to compare because the authors often only refer to the Al to Zn ratio in the start mixture. The resistivity values of the order of 10^{-4} Ωcm obtained for thin films for materials via the sol-gel method after tempering[20] and via a magnetron-sputtering method[2,21] show minima close to 1% and 3% in Al to Zn ratio, respectively. These values indicate that competitive materials can be found also via the sol-gel method.

Here we want to focus less on the preparation but rather on the structural analysis of the materials from sol-gel methods which yield complex materials at the different stages of synthesis. Our analysis aims at a deeper understanding of doping induced defects and the mechanisms which will influence electrical conductivity. In this respect early findings[2] are important which showed that AZO films behave as degenerate n-type semiconductors where the dopant Al acts as an efficient electron donor. Furthermore it was found that resistivity[2] is limited by grain-boundary scattering and ionized impurity scattering which is in line with finding a minimum of the resistivity as a function of Al dopant concentration.

With respect to the Al doping-induced disorder and the Al defects, several competing, if not incompatible, structural models have been proposed. As far as we know, only point defects have been considered so far, although a much wider variety of defects, like edge and screw dislocations or planar

and volume defects, seem to be possible.[22,23] Table 1 gives an overview of the suggested defects. Most works considered aluminium as substitution for zinc ($\mathbf{Al_{Zn}^{\bullet}}$) to be a likely defect. Two further possibilities of Al incorporation into the ZnO lattice being discussed[24,25,18] are an "octahedrally-coordinated" interstitial site $^{\mathbf{VI}}\mathbf{X_i}$, which we will denote as $\mathbf{Al_{\mathit{i,Oh}}}$, and a "tetrahedrally-coordinated" interstitial $^{\mathbf{IV}}\mathbf{X_i}$, here denoted as $\mathbf{Al_{\mathit{i,Td}}}$. Next to supposably neutral defects,[26] where three Zn^{2+} neighboring cations are replaced by two Al^{3+} cations and one Zn-vacancy (alias $\mathbf{[Al_2 \mathit{V}_{Zn}]}$), also hydrogen bearing defects, namely $\mathbf{OH_O^{\bullet}}$,[17] were suggested, resulting from exposure of the samples to hydrogen. The list is completed by $\mathbf{[Al_2^{3+}O_i^{2-}]}$ (O^{2-} interstitial complexed by two Al^{3+}),[27,28] which was surmised mainly from conclusion by analogy of the ZnO:Ga and ZnO:Al system. Other defects ($\mathbf{Zn_i^{\bullet\bullet}}$, $\mathit{V_O''}$, …) have been discussed as well, but their relevance seems rather unlikely in case of the chemically "soft" sol-gel based syntheses. Moreover side-phase formation has been discussed. It should be noted that on the basis on the measurement of macroscopic properties it is rather difficult to provide solid evidence for or against a defect.

Clearly there is a need for an application of analytical methods which help to distinguish between the above presented defects in AZO. A suitable method with a resolution power on an atomic scale is solid-state NMR. Thus ^{27}Al NMR has been applied to AZO in bulk form,[28,29,26,30] nano-particles[19] and in form of nano-wires[18,24] to elucidate how the dopant integrates into the ZnO structure. Important observations were that ^{27}Al NMR resonance in the metallic AZO experiences has a chemical shift value outside the ordinary regime which is typical for Al in metals[29,28] and for a different synthetical route a solubility limit of Al in ZnO[26] has been suggested accompanied with the formation of a crystalline side-phase of $ZnAl_2O_4$ at temperature above 800°C. ^{27}Al solid-state NMR straight away indicates that even for bulk materials several Al environments may exist which doesn't match the simple picture of a single phase being homogeneously doped with Al on a single type of point defect.

In order to obtain ^{27}Al NMR fingerprint of different suggested point-defects, symmetry arguments could be used, which make predictions about the ^{27}Al NMR lineshape: If the 3-fold axis of the Zn site is conserved, a rather simple lineshape function for a Al filled Zn vacancy $\mathbf{Al_{Zn}^{\bullet}}$ is expected. However it is clear that the ZnO host lattice will undergo local structural changes in the vicinity of these defects, which may as well reduce the site symmetry of the Al position. In fact both the distortion and the conservation of the 3-fold axis can be found in literature for different dopants.[31,28,32,33] While quantum chemical calculations have proven their potential to study the structure and energetics of defects in

ZnO,[31–38] what is missing is the calculation of NMR properties for the suggested defect models.

Table 1: Proposed defects in ZnO:Al in Kröger-Vink notation[39] and their effect on conductivity

defect type	effect on conductivity	Ref.
$Al_{Zn}^{\bullet}$ (+1e^-)	increase by *n*-doping	2,17,24,26,28,40
$Al_{i,Oh}^{\bullet\bullet\bullet}$ (+3 e^-)	increase, Al interstitial octahedrally coordinated to O sites.	24
$Al_{i,Td}^{\bullet\bullet\bullet}$ (+3 e^-)	increase, Al interstitial, tetrahedrally coordinated to O sites.	24
$Zn_i^{\bullet\bullet}$ (+2e^-)	increase (naturally occurring in ZnO)	2,26,27
V_O''	increase (naturally occurring in ZnO), upper limit for ZnO_{1-x} is x= 0.0003 and therefor probably irrelevant as compared to other dopants	2,26,27
[$Al_2^{3+}V_{Zn}$] (+0e^-)	none or decrease	26
[$Al_2^{3+}O_i^{2-}$] (+0e^-)	none or decrease	40,28
$H^{\bullet}/OH_O^{\bullet}$ (+1e^-)	increase (unintentional doping)	17,32
side-phase	$ZnAl_2O_4$ spinel (microcrystalline, formed at higher temp.), decrease	26,18,24,15
side-phase	Al_2O_3 (amorphous), decrease	15

In this contribution we want to elucidate what happens to the dopant Al in nanoscale aluminium doped ZnO (AZO). To this end nano-particles with a narrow size-distribution are prepared using the polyol-method[41] and formed into transparent conductive films at temperatures below 500°C. Their size-distribution, composition and electrical properties are characterized by standard techniques. Due to the rather low processing temperatures we expect the AZO materials to be more complex both in composition and morphology. For this reason we base our NMR study not only on ^{27}Al as previous NMR studies did but also on ^{13}C and ^{1}H and correlations between these nuclei. For the interpretation of the NMR data we further provide reference values of NMR properties for different Al point-defect models by quantum chemical calculations.

Experimental Details

Synthesis and particle characterization

Aluminium-doped zinc oxide (AZO) nanoparticles were prepared according to the following recipe: 4.56 mmol of $Zn(CH_3COO)_2{\cdot}2H_2O$ were dissolved in 50 ml DEG together with 0.05, 0.23 or 0.92 mmol of $AlCl_3{\cdot}6H_2O$ which corresponds to a molar ratio Al:Zn of 1, 5 and 20%, respectively. Subsequently, 1 ml deionized H_2O was added. The mixtures were heated under Argon atmosphere to

200°C in a laboratory microwave oven with magnetic stirring (MLS rotaprep: 1.2 kW, 2.45 GHz; fiber optic as well as pyrometer for temperature control). To improve the material crystallinity, the temperature was maintained for 30 min. As-prepared AZO suspensions from the 1, 5 and 20 mol % aluminium sols were colloidally stable for months. The suspensions exhibit a slight blueish shade and transparent appearance. As a reference, non-doped ZnO was synthesized similarly. As-prepared nano-scale AZO powders can be separated from the suspension by centrifugation and drying. More details regarding the synthesis have been described elsewhere.[41] These as-prepared AZO powders were heated for 30 min in air at 400°C to burn away remaining DEG, and subsequently reduced with forming gas (H_2/N_2 = 10/90%) for 60 min at 400°C to increase conductivity. To minimize the influence of grain boundaries when evaluating the electrical resistance, powder samples were pressed to pellets with an IR pressing tool for 15 min at 50 kN (Specac stainless steel pressing tool, 13 mm in diameter; Specac hydraulic laboratory press). The thickness of these pellets was calculated based on materials weight and density (5.6 g cm^{-3}), assuming a space filling of 74% with close-packed nanocrystals.

Dynamic light scattering (DLS) of DEG suspensions was measured in polystyrene cuvettes with a Nanosizer ZS from Malvern Instruments. Measurements were conducted on suspensions sufficiently diluted to deter particle-to-particle interactions, which was determined through a dilution series. *Transmission electron microscopy (TEM)* was performed with a Philips CM200 FEG/ST microscope at an acceleration voltage of 200 kV. Samples were prepared by ultrasonic nebulization of an ethanolic dispersion on a Cu grid with a holey carbon film. *X-ray powder diffraction (XRD)* was carried out with a Stoe STADI-P diffractometer operating with Ge-monochromatized Cu-K_α radiation. *Brunauer-Emmett-Teller (BET)* analysis of as-prepared powder samples was carried out with a BELSORP-mini II from BEL, applying N_2 as adsorbate. *Fourier-transform-infrared (FT-IR) spectra* were recorded with a Vertex 70 FT-IR spectrometer from Bruker Optics. The transmittance of pellets consisting of 1 mg sample powder and 300 mg KBr was measured in a wavenumber interval of 7000−370 cm^{-1}. *Quantitative elemental analysis* of the aluminium content was carried out by a commercial microanalytical laboratory, Mikroanalytisches Labor Pascher, Remagen, Germany. The *sheet resistivity* of pellets and films was measured via four-point probing using a Keithley system (485 Autoranging Picoammeter, 199 System DMM/Scanner, 230 Programmable Voltage Source). The electrodes were placed in a row and at a distance of 1.0 mm to each other. To calculate the sheet resistivity, a geometrical correction factor equal to $\pi/\ln 2$ was applied.

Solid-State NMR

All magic-angle-spinning (MAS) NMR experiments were carried out at ^{27}Al, ^{13}C and ^{1}H frequencies of 130.31, 125.75 and 500.13 MHz, respectively, on a Bruker Avance-III NMR spectrometer equipped with a commercial 1.3, 2.5 or 4 mm triple-resonance probe. The chemical shift values reported for ^{1}H, ^{13}C refer to 1% tetramethylsilane (TMS) in $CDCl_3$ and ^{27}Al refer to a 1.1 mol kg^{-1} solution of $Al(NO)_3$ in D_2O on a deshielding scale. The ^{1}H resonance of 1% tetramethylsilane in $CDCl_3$ served as an external secondary reference using the Ξ-values for ^{13}C and ^{27}Al as reported by the IUPAC.[42] Saturation combs were applied prior to all repetition delays. The one-dimensional (1D) ^{1}H MAS NMR was acquired with a 90° pulse length of 2.5 μs, a recycle delay τ_{RD} of 4.0 s and at a sample spinning frequency ν_{MAS} of 50 kHz. Typical 90° pulse lengths for the ^{27}Al central transition were 10.0 μs. The 1D ^{27}Al MAS experiments were conducted using τ_{RD} values of 3.0 – 64.0 s, at a sample spinning frequency ν_{MAS} of 10 kHz. In the spin echo sequence, coherence transfer pathways were selected with a 16-step phase cycle. The ^{13}C{^{1}H} ramped cross-polarization[43] under MAS conditions (ramped CPMAS) was performed at a ν_{MAS} of 6 kHz, a τ_{RD} of 3.0 s and a contact time of 1.0 ms.

A triple-quantum ^{27}Al MQMAS 2D spectrum was acquired using a three-pulse sequence with a zero-quantum filter,[44] a repetition delay of 16.0 s, and rotor-synchronized sampling of the indirect dimension. Phase cycling involved the States method[45] for acquisition of pure absorption line shapes. The second-order quadrupolar effect parameter (*SOQE*) and isotropic chemical shift values were determined by moment analysis[44,46] from the extracted rows of the sheared MQMAS spectrum. The selective pulses for the excitation of the ^{27}Al central transition used a nutation frequency ν_{rf} of 50 kHz in the MQMAS and also the REDOR-experiments presented below.

For the C-REDOR experiment, repetition delays τ_{RD} were set to 8.0 s and 1024 transients were accumulated for spectrum. The experiment used CX^{1}_{X} symmetries and a Post C-element[47,48] which corresponds to a ^{1}H nutation frequency ν_{rf} of 50 kHz at a spinning frequency ν_{MAS} of 25 kHz. The C-REDOR data were plotted as $\Delta S/S_0$ against the universal dephasing time τ_{uds},[49,50] which is a pulse sequence-independent time scale defined from the product $|\kappa|\tau$ of the magnitude of the scaling factor κ and the dipolar dephasing time τ. The scaling factor[51] κ for the REDOR sequence[52] in the δ-pulse limit and the C-REDOR are 0.367553 and 0.24503, respectively. A rough estimate for an effective dipolar coupling $\nu(^{27}\mathrm{Al}, ^{1}\mathrm{H})$ was obtained via fitting of the initial part of the C-REDOR with the help of the SIMPSON package[53,54] in a two-spin approximation neglecting quadrupole coupling and

chemical shift.

For 2D ^{27}Al{^{1}H} heteronuclear-correlation 2D MAS NMR spectroscopy, we converted the PRESTO-III pulse-sequence[55] (Figure 1) into a 2D correlation experiment by encoding the chemical shift of ^{1}H during extra $\pi/2-t_1-\pi/2$ block, which is followed by a short zero-quantum filter of a few μs. Proton decoupling was implemented using continuous wave (cw) decoupling with a rf field strength corresponding to 100 kHz. The nutation frequency for the selective pulses applied to the ^{27}Al central transition was 50 kHz. The $R18_1^7$ recoupling sequence used a ^{1}H nutation frequency of 45 kHz for the R-elements which consisted of simple π-pulses as described in the original PRESTO publication.[55] The 2D ^{27}Al{^{1}H} experiment (Figure 7) on AZO-ap (1.8 %) was performed at a spinning frequency of 10 kHz using 2048 transients/FIDs, a 4.0 s recycle delay, rotor synchronized t_1 increments and 2D data acquisition according to the States methods.[45] Coherence transfer pathway selection was achieved with an 4 step phase-cycle. The advantage of PRESTO over cross-polarization based HETCOR experiments is that the pulses on the ^{27}Al channel only require information about a selective central-transition pulse, while the Hartmann-Hahn condition of the CP experiment is more difficult to set up. This is why we were able to acquire 2D HETCOR spectra with a good signal/noise, despite Al being only a dopant occurring in the percent range. The length of the recoupling intervals, τ_1 and τ_2 were 500.0 μs (Figure 1).

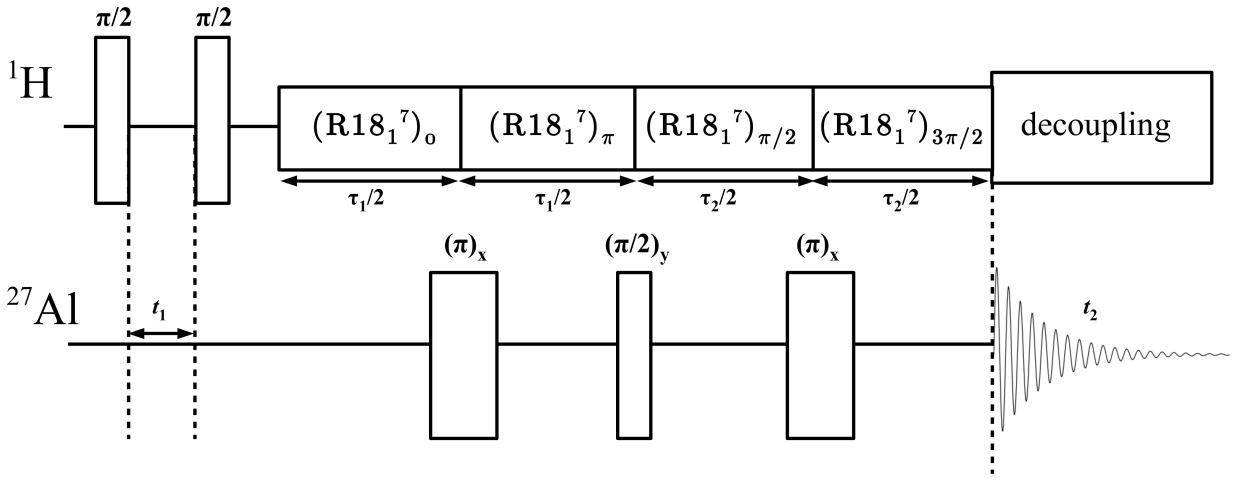

Figure 1: 2D PRESTO-III pulse sequence for ^{27}Al{^{1}H} HETCOR experiments; recoupling periods $\tau_1=\tau_2=500.0\mu s$ are denoted by $R18_1^7$, which is an R-symmetry pulse sequence where the R-element is a simple π-pulse, the recoupling sequence is used as described in detail in reference.[55]

Computational Details

Quantum chemical structure optimizations were performed in order to predict the local structure at the (potential) defects: Al_{Zn}, $Al_{i,Td}$, $Al_{i,Oh}$, as well as the defect combinations $[Al_2V_{Zn}]$, $[Al_{i,Td}V_{Zn}]$, $[Al_{i,Oh}V_{Zn}]$. Calculations were performed by a supercell approach under periodic boundary conditions with the VASP program,[56–59] version 4.6.28, using the projector augmented plain wave (PAW) method.[60,61] A Γ-centered *k*-point mesh[62] with four points in each direction (4x4x4) was used and the plane wave energy cutoff was set to 500 eV. The PBE density functional[63] was used with the standard pseudo potentials delivered for PBE/PAW with VASP. Supercells were chosen as 3x3x2 expansions of the *wurtzite*-like ZnO cell[64] (space group $P6_3mc$, ICSD 76641) with one of the mentioned defects included at a time. Symmetries of the doped supercells were initially maintained at $P3m1$ (No. 156) for Al_{Zn}, $Al_{i,Td}$, $Al_{i,Oh}$ during the optimizations, but were released subsequently to $P1$ (No 1) by slight displacements of the dopant in order to check for Jahn-Teller-distortions[65] of lower energy. The $[Al_2V_{Zn}]$-defect can occur in three different variants in ZnO (see Figure 11), all of which were treated in space group $P1$. The defects $[Al_{i,Td}V_{Zn}]$ and $[Al_{i,Oh}V_{Zn}]$ were treated in $P1$ as well. For each defect various partial structure optimizations were performed (Al-atoms only, Al plus 1st coordination sphere, Al plus 1st and 2nd coordination sphere) as well as full optimizations of all fractional coordinates to investigate the convergence of the structural relaxation. Supercell parameters were kept constant at $a = b = 9.7485$ Å, $c = 10.4138$ Å in all calculations. Optimizations were considered as converged when the energy between two subsequent steps was below 10^{-7} eV and the residual forces were converged to 10^{-6} eV/Å. For Al_{Zn} the number of electrons in the supercell was varied from its formal value by ±1 in order to investigate structural effects of electron doping. For all three types of doping, spin-polarization free calculations have been performed. Deviations from charge neutrality within a unit cell were compensated by a homogeneously distributed counter charge (*jellium background*). No compensation mechanism for higher electrical moments was used.

Moreover, the ^{27}Al NMR properties of the optimized sites were calculated, i.e. the electric field gradient tensor (EFG, $\boldsymbol{q}$) and the absolute magnetic shielding tensor $\boldsymbol{\sigma}$. To this end we made use of the *Extended Embedded Ion Method* (EEIM),[66] an embedded cluster approach derived from the Embedded Ion Method (EIM),[67,68] whose basic feature is the embedding of the quantum cluster (QC) in a self-consistent point charge field that simulates the environment of an ideal crystal in the electrostatic approximation, which is well suited to the treatment of doped materials at low doping levels.[69] Because

the EFG as well as the chemical shift is a local quantity,[70] embedded cluster methods are also suitable for its calculation.[71] For doped crystals we propose a two-step procedure analogous to the one for σ in described in ref. 69: In the first step, the embedding point charges are obtained for an ideal (i.e. non-defective) crystal/QC, where the usual self-consistent procedure of EEIM as described in ref. 66 is employed. The optimized atomic charges for Zn and O are ±1.60734·*e*, respectively. In the second step, the QC is modified to contain one of the (relaxed) defect sites close to its center, as well as an outer region in which the atomic sites of the ideal crystal are left unperturbed.† As the charge q_{QC} of the modified QC cannot be determined exactly, it is set to a value that allows a closed shell calculation and, at the same time, is close to the sum of the expected fragment charge according to the self-consistent charges determined in the first step and the assumed defect site charge. Formal charges can be used for lowly charged defect sites, since the EEIM seems to tolerate small charge misfits of the QC.[69] Finally, the calculation of EFG and NMR parameters is performed and their variability on q_{QC} is investigated. The detailed setup of QCs is given in the supplementary information (SI).

The hybrid density functional mPW1PW[72] as implemented in the GAUSSIAN 03 (g03) program[73] was used for the electronic structure calculations (ESCs) in EEIM. Population analysis and atomic net charges were determined by the NBO 5.0 program.[74] A locally dense AO basis of gaussian functions was defined based on a distance criterion with basis functions up to 6-311G(3df,3pd)[75,76] near the defect site and gradually decreasing quality down to CEP-4G[77] at farthest distances. The convergence of the EFG for Al_{Zn} was checked with respect to the AO set by using a pcS-3 set[78] with decontracted core orbitals, and with respect to the quadrature grid as well as the SCF convergence criteria. Only restricted wave functions were allowed. From the EFGs principal axis values $|V_{zz}^{PAS}| \geq |V_{xx}^{PAS}| \geq |V_{yy}^{PAS}|$ we calculate the experimentally observable nuclear quadrupole coupling constant C_q, the asymmetry parameter η_q and the second order quadrupolar effect *SOQE* according to[79,80]

$$C_q = \frac{e V_{zz}^{PAS} Q_s}{h} \quad , \tag{1}$$

†Thus the periodicity of defects present in supercell approaches is avoided. In principle, structural relaxations of the defect site can also be performed within the EEIM, if the QC region is chosen large enough. Atoms at the QC boundary must not be relaxed because their direct neighborhood to point charges can result in unrealistic structures.[69]

$$\eta_q = \frac{V_{yy}^{PAS} - V_{xx}^{PAS}}{V_{zz}^{PAS}} \quad \text{and} \tag{2}$$

$$SOQE = C_q \sqrt{1 + \frac{\eta_q^2}{3}} \tag{3}$$

where $Q_s=Q/e$ is the *spectroscopic nuclear quadrupole moment*,[81] which amounts to 146.6 mb (1 mb = 10^{-31} m^2) for ^{27}Al, e is the electric charge unit and h Plank's constant. Note, that the EFG tensor elements in g03 are given with the sign convention $V_{ij} = -\partial^2 V/(\partial i \partial j)$, $i,j \in \{x,y,z\}$, and in atomic units, whereas the V_{ii}'s in eqns. 1 and 2 use an opposite sign and SI units (Vm^2). Conversion from the traceless EFG tensor eigenvalues in g03 to the values used here is achieved by $V_{ii}/(\mathrm{Vm}^2) = -9.717361\times10^{21}\times V_{ii}/(\text{a.u.})$.

Absolute nuclear magnetic shielding tensors σ were calculated using the GIAO formalism.[82] For the derivation of a conversion equation from absolute magnetic shieldings σ (^{27}Al) to chemical shift values δ (^{27}Al) we used solid α-Al_2O_3 as a secondary reference, whose experimental isotropic chemical shift has been determined to $\delta_{iso}^{\exp}$ =18.8 ppm,[83] and to 16.0 ppm.[80] We used the first value in the conversion equation 4 for a given sample *s*.

$$\delta^{calc}(s) = \sigma_{iso}^{calc}(\alpha - Al_2O_3) - \sigma^{calc}(s) - \delta_{iso}^{\exp}(\alpha - Al_2O_3) \tag{4}$$

$\sigma_{iso}^{calc}(\alpha - Al_2O_3)$ is calculated with the same quantum chemical model and basis functions as $\sigma^{calc}(s)$, as far as possible, to cancel out systematic basis set errors. An EEIM procedure resulted in σ_{iso}^{calc} (α-Al_2O_3)=578.68 ppm for 6-31G*, 557.78 ppm for 6-311G(3df,3pd), 555.98 ppm for pcS-3 and 555.66 ppm for uncontracted pcS-3. Details are given in the SI. The similarity between 6-311G(3df,3pd) and (uncontracted) pcS-3 shieldings indicates that the basis expansion is sufficiently converged.

Results and Discussion

Characterization of as-prepared AZO nanoparticles

AZO nanoparticles were prepared via a polyol-mediated synthesis. Diethylene glycol (DEG) was used as the polyol and allowed to efficiently control the nucleation and growth of the nanoparticles.[84] Moreover, crystalline nanoparticles can be gained due to the high boiling-point of the polyol (248°C). To investigate particle size and size distribution of the as-prepared AZO samples (AZO-ap), dynamic light scattering (DLS) and electron microscopy were involved (Figure 2). Accordingly, suspensions in DEG exhibit a hydrodynamic diameter of about 12 nm and a narrow size distribution. Electron

microscopy shows nanoparticles with spherical shape (Figure 2). Based on a statistical evaluation of >200 particles, mean diameters of 10 nm were determined. High-resolution TEM images, furthermore, point to the crystallinity of the AZO nanoparticles. Lattice fringes with distances of 2.84 Å are well in accordance with ZnO (zincite: (100) with 2.81 Å).[85] X-ray powder diffraction pattern confirms the presence of crystalline ZnO (Figure 3). Based on the Scherrer formalism, average crystallite sizes of 8-12 nm can be deduced, which fit well with the results stemming from DLS and TEM. Thermogravimetry (TG) was performed to study the thermal behavior of the as-prepared AZO nanoparticles and to quantify the amount of DEG adhered on the particle surface. Here, a continuous weight-loss of 2.6 % was observed between 200 and 400°C (Figure 3). When considering the boiling point of DEG, this weight-loss can be attributed to DEG adhered as a surface-capping on the particle surface. This view and explanation is also well in accordance with previous studies.[22,37]

The chemical composition and concentration of the aluminium doping was investigated by energy-dispersive X-ray analysis (EDX) as well as by wet-chemical analysis. According to EDX, Al/Zn-ratios of 0.8, 1.0 and 5.3 mol-% were obtained for the samples with a formal Al-dopage of 1.0, 5.0, and 20.0 mol-% provided in the mixture of the starting materials. Although Al^{3+} is incorporated and the real ratio correlates with the formal one, a significant percentage of the Al^{3+} obviously remains in solution so that the real doping of the solid nanomaterials is lower than expected. Wet-chemical analysis resulted in 1.0, 1.8 and 4.6 mol-%. In the following the as-prepared AZO samples are therefore indicated as AZO-ap (x % with x = 1.0, 1.8, 4.6).

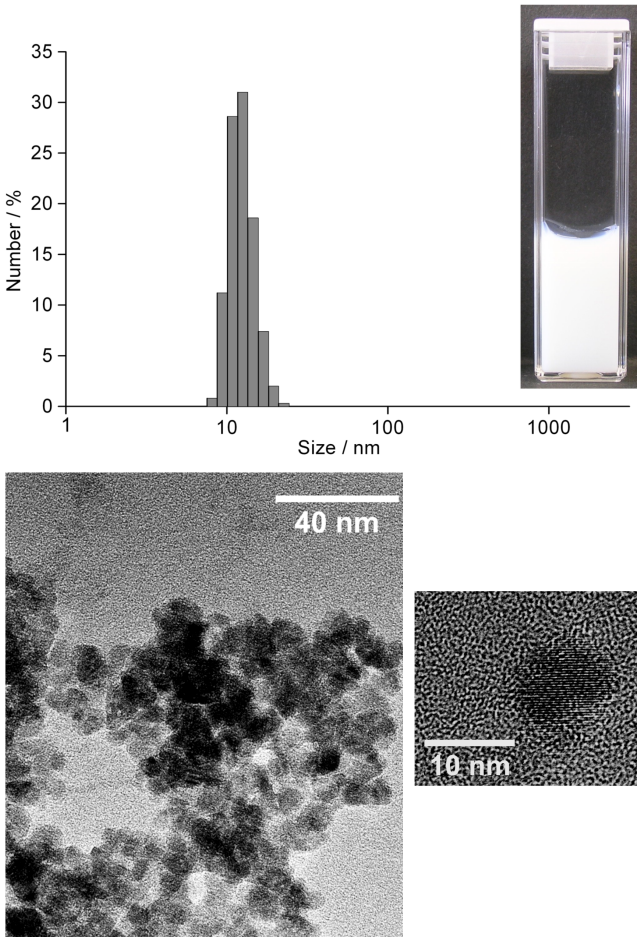

Figure 2: Particle properties of the as-prepared AZO nanoparticles: photo of suspension in ethanol; size and size distribution according to DLS, TEM and HRTEM.

To investigate the conductivity of the AZO-ap samples, powdered samples were first pressed to pellets. This measure guarantees a close contact between the individual nanoparticles. Thereafter, the pellets were investigated by four-point probing. AZO-ap samples do not show any measurable conductivity at all (Table 2). On the one hand, this is due to DEG as the surface-capping that hinders the interparticular charge transport. Aiming at conductive AZO, the samples were first sintered, under oxidizing conditions in air at 400°C for 30 min to remove the surface capping and to enable conductive surface contacts between the particles. These samples are indicated as AZO-ox (Table 2). Subsequently, free charge carriers are established by a second reductive heating in forming gas at 400°C for 1 h (indicated as AZO-red, Table 2). Both thermal procedures – the oxidative as well as the reductive step – are widely applied for processing transparent conductive oxides.[86] To study structural and morphological effects, the AZO samples were finally heated in air at 800°C for 0.5 h (indicated as AZO-800, Table 2).

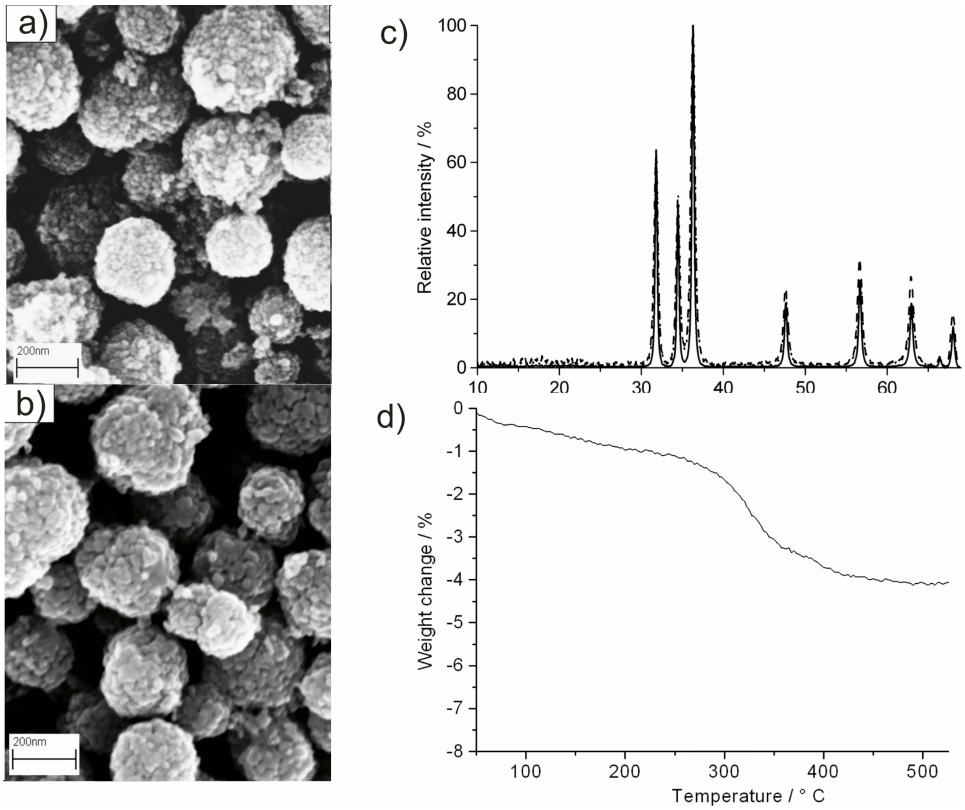

Figure 3: Thermal properties of the AZO nanoparticles: a) SEM image of the as-prepared, agglomerated nanoparticles; b) SEM image of agglomerated nanoparticles subsequent to oxidative and reductive treatment at 400°C; c) XRD pattern (dotted: as-prepared; dashed: 400°C; straight: 800°C); d) thermogravimetry.

To evaluate the sintering behavior and the particle size during the heating procedures, the samples AZO-ox and AZO-red were characterized by X-ray powder diffraction to determine the crystallite size via the Scherrer formalism (Table 2). Surprisingly, the crystallite size remains almost constant during the oxidative as well as during the reductive heating procedure. Only the samples treated at 800°C show a significant increase of the crystallite size (Table 2). Furthermore, N_2 sorption analysis was involved to study the sintering behavior. Accordingly, the BET surface approximately drops by a factor of 2 when heating to 400°C (Table 2) which again indicates a certain sintering of the nanoparticles. This finding is also in accordance with agglomerates of nanoparticles that are visible on SEM images subsequent to sintering at 400°C (Figure 3). In sum, XRD, BET and SEM validate that even the agglomerated AZO samples obtained after the oxidative and reductive heat treatment are still nanoscaled and with diameters below 50 nm. The lowest sheet resistance was finally measured for AZO-red (1.0 %) and AZO-red (1.8 %) with values of 160 and 170 Ω/□, respectively (Table 2).

Table 2: Overview of thermal and analytical characterization of AZO samples; "∞" indicates a sheet resistance which was too high to be measured.

type of sample	crystallite size (XRD) /nm	specific surface (BET) /m^2g^{-1}	Sheet resistance /(Ω/□)
AZO-ap (1.0 %) air, 70 °C, 12 h	17	42	∞
AZO-ox (1.0 %) air, 400 °C, 0.5 h	18	21	∞
AZO-red (1.0 %) 1. air, 400 °C, 0.5 h 2. N_2/H_2, 400 °C, 1.0 h	18	19	160
AZO-ox-800 (1.0 %) air, 800 °C, 0.5 h	30	7	∞
AZO-ap (1.8 %) air, 70 °C, 12 h	13	43	∞
AZO-ox (1.8 %) air, 400 °C, 0.5 h	16	28	∞
AZO-red (1.8 %) 1. air, 400 °C, 0.5 h 2. N_2/H_2, 400 °C, 1.0 h	16	22	170
AZO-ox-800 (1.8 %) air, 800 °C, 0.5 h	23	11	∞
AZO-ap (4.6 %) air, 70 °C, 12 h	18	33	∞
AZO-ox (4.6 %) air, 400 °C, 0.5 h	21	40	∞
AZO-red (4.6 %) 1. air, 400 °C, 0.5 h 2. N_2/H_2, 400 °C, 1.0 h	20	28	340
AZO-ox-800 (4.6 %) air, 800 °C, 0.5 h	30	13	∞

Solid-State NMR characterization

Recently solid-state ^{27}Al MAS NMR studies[17,18,20,21] indicated that the Al environment are far less uniform if nanoscale AZO is synthesized via a colloidal route from a liquid phase. Here we use ^{13}C and ^{1}H MAS NMR to elucidate the immediate environment of the DEG molecules in the particle shell. In addition, simple ^{27}Al NMR allows us to distinguish different Al environment by their connectivity numbers, which will further be corroborated by ^{27}Al MQMAS experiments. Experiments based on the heteronuclear dipolar interaction (PRESTO and REDOR) between ^{1}H and ^{27}Al finally allows us to decide which Al environments are related to the particle shell or side-phases. A sensitive indicator for electrical conductivity is spin-lattice relaxation: ^{27}Al spins in the metallic particle are supposed to show Korringa behavior.

^{27}Al NMR - aluminium environments: The local environment of the Al ions in the aluminium doped zinc oxide nanoparticles is studied by ^{27}Al MAS NMR. The ^{27}Al MAS NMR spectrum of AZO-ap (1.8 %) shows four partially overlapping components (Figure 4, top). An assignment can be made on

the basis of a strong correlation between the observed chemical shift δ_{obs} value and the coordination number of the Al atom.[87] Hence the peak at 82.6 ppm is assigned to an aluminium atom coordinated to 4 oxygen atoms $\left(Al_A^{(IV)}\right)$, the two broad peaks from around 80 to 50 ppm and 50 to 30 ppm are assigned to four- $\left(Al_B^{(IV)}\right)$ and fivefold $\left(Al^{(V)}\right)$ coordinated aluminium sites, respectively and the peak at 12.6 ppm to an Al site coordinated to six oxygen atoms $\left(Al^{(VI)}\right)$. The linewidth (4.8 ppm) and the spin-lattice relaxation time T_1 (4.9 s) (Table 3) of the $Al_A^{(IV)}$ signal are both very different from those of the other signals. Note, that the lineshape of a ^{27}Al NMR resonance in a solid can be significantly broadened by distributions of environments in disordered or amorphous materials and/or by the quadrupolar interaction which may vanish however when the nucleus is a site of high point-group symmetry, e.g. T_d or O_h. The rather small linewidth for $Al_A^{(IV)}$ strongly indicates a highly ordered, crystalline environment.[18,19] Hence, we assign it to a fourfold coordinated Al at a zinc position within the ZnO crystal structure, i.e. a Al_{Zn} point defect in Kröger-Vink notation. In contrast to the $Al_A^{(IV)}$ signal, the $Al_B^{(IV)}$, $Al^{(V)}$ and $Al^{(VI)}$ signals have broad linewidths and short T_1 times (Table 3) which are in agreement with a highly disordered or asymmetric environments. Thus 1D ^{27}Al MAS NMR gives first evidence that the Al dopant is distributed over four different environments.

In a second step we compare the ^{27}Al MAS NMR spectra of three different AZO samples (Table 2), namely, as-prepared AZO (AZO-ap, 1.8 %), with a sample subsequently dried at 400 °C in air (AZO-ox-400, 1.8 %) and a sample (AZO-red, 1.8 %) which subsequent to drying was subject to a reductive atmosphere (forming gas H_2/N_2). In the ^{27}Al MAS NMR (Figure 4) hardly any changes of the as-made sample upon drying can be observed, however there is a drastic change once the sample is subject to a reductive atmosphere, when the sharp $Al_A^{(IV)}$ peak at 82.6 ppm vanishes and a new broad peak with a similar peak area at 165 ppm occurs. This observation is in line with the measured electrical properties of the three samples for which only the reduced sample shows a notable conductivity. We assign the broad peak which is far outside the ordinary range of dielectric oxides,[17,41,42] to Al in ZnO which has become metallic by the reductive treatment and thus is subject to a Knight shift from the conduction electrons, as observed in previous ^{27}Al NMR studies of AZO.[18,29] However, in contrast to an NMR study of AZO fibers[18] we observe the Knight shifted peak only after the reductive treatment (AZO-red). Because qualitatively, the only change observed upon the reductive treatment happens with respect to

the sharp peak $Al_A^{(IV)}$, which we previously assigned to Al_{Zn} in the ZnO crystal structure, we conclude that the peaks for the other Al environments remain in a non-metallic environment. Independent evidence for this interpretation is provided below by experiments based on the heteronuclear dipolar coupling between ^{27}Al and ^{1}H and by a characterization of the relaxation behavior.

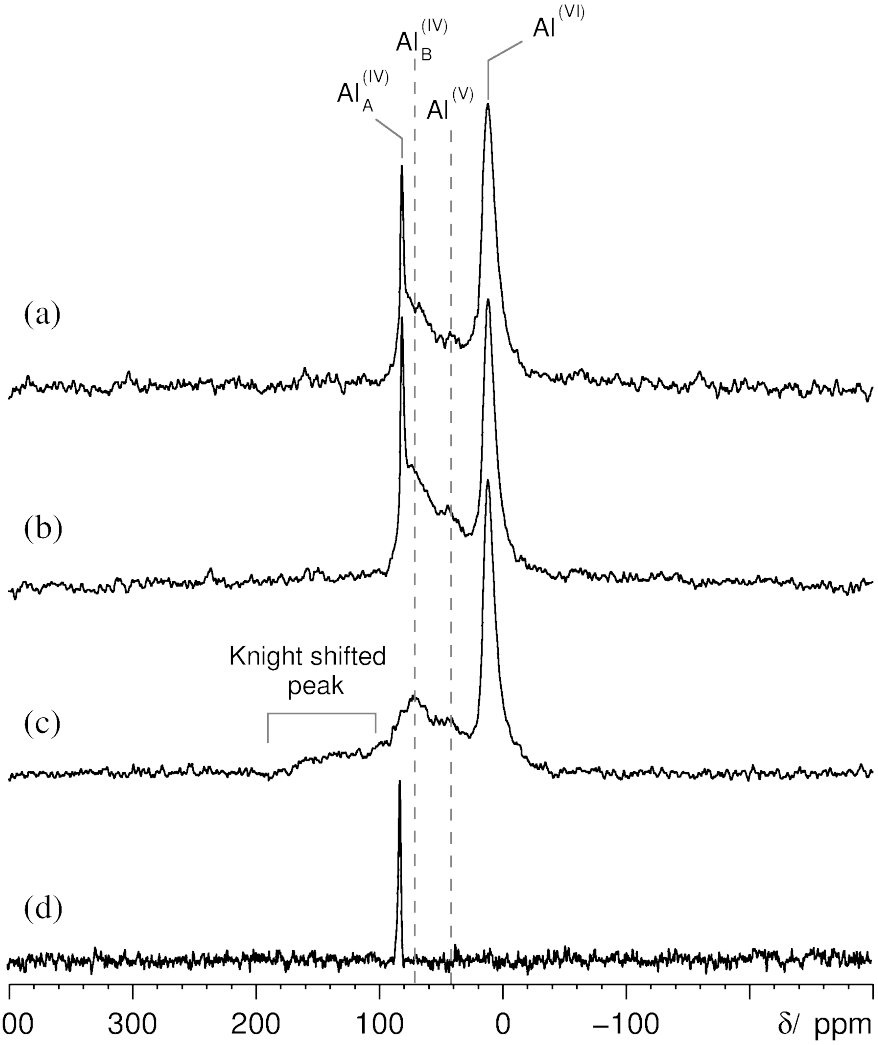

Figure 4: ^{27}Al spin echo MAS NMR spectra of AZO (1.8 mol %) (a) as-prepared aluminium-doped zinc oxide; (b) aluminium doped zinc oxide heated to 400°C in air; (c) reduced via forming gas processing; (d) difference spectrum of as-prepared AZO obtained by subtraction of two directly excited spectra with different recycle delays τ_{RD} of 64 s and 0.9 s; all experiments were acquired at a spinning speed ν_{MAS} of 10 kHz in a magnetic field of 11.74 T; approximately same amount of sample was packed into the rotor; spectra (a), (b) and (c) were acquired with similar experimental conditions and plotted approximately on the same y-scale.

Table 3: ^{27}Al NMR chemical shift and the spin–lattice relaxation time T_1 of different AZO samples; the Al doping percentage in braces refers to the Al/Zn molar ratio determined by "wet" chemical analysis for the bulk material.

type of sample	isotope	signal	δ_{obs}/ppm	T_1/s
ZnO:Al (AZO-ap, 1.0 mol %)	^{27}Al	$Al^{(VI)}$	12.6	0.02
		$Al^{(V)}$	30-50	0.2
		$Al_B^{(IV)}$	50-80	0.3
		$Al_A^{(IV)}$	82.6	7.9
ZnO:Al (AZO-ox, 1.0 mol %)	^{27}Al	$Al^{(VI)}$	12.6	0.06
		$Al^{(V)}$	30-50	0.16
		$Al_B^{(IV)}$	50-80	0.25
		$Al_A^{(IV)}$	82.6	7.5
ZnO:Al (AZO-red, 1.0 mol %)	^{27}Al	$Al^{(VI)}$	12.6	0.04
		$Al^{(V)}$	30-50	0.2
		$Al_B^{(IV)}$	50-80	0.29
		Knight shifted peak	165.0	0.75
ZnO:Al (AZO-ap, 1.8 mol %)	^{27}Al	$Al^{(VI)}$	12.6	0.018
		$Al^{(V)}$	30-50	0.16
		$Al_B^{(IV)}$	50-80	0.29
		$Al_A^{(IV)}$	82.6	7.8
ZnO:Al (AZO-ap, 4.6 mol %)	^{27}Al	$Al^{(VI)}$	12.6	0.06
		$Al^{(V)}$	30-50	0.17
		$Al_B^{(IV)}$	50-80	0.2
		$Al_A^{(IV)}$	82.6	8.0
ZnO:Al (AZO-ox-800, 4.6 mol %)	^{27}Al	$Al^{(VI)}$	12.6	3.1
		$Al^{(V)}$	30-50	1.8
		$Al_B^{(IV)}$	50-80	0.9
		$Al_A^{(IV)}$	82.6	5.4

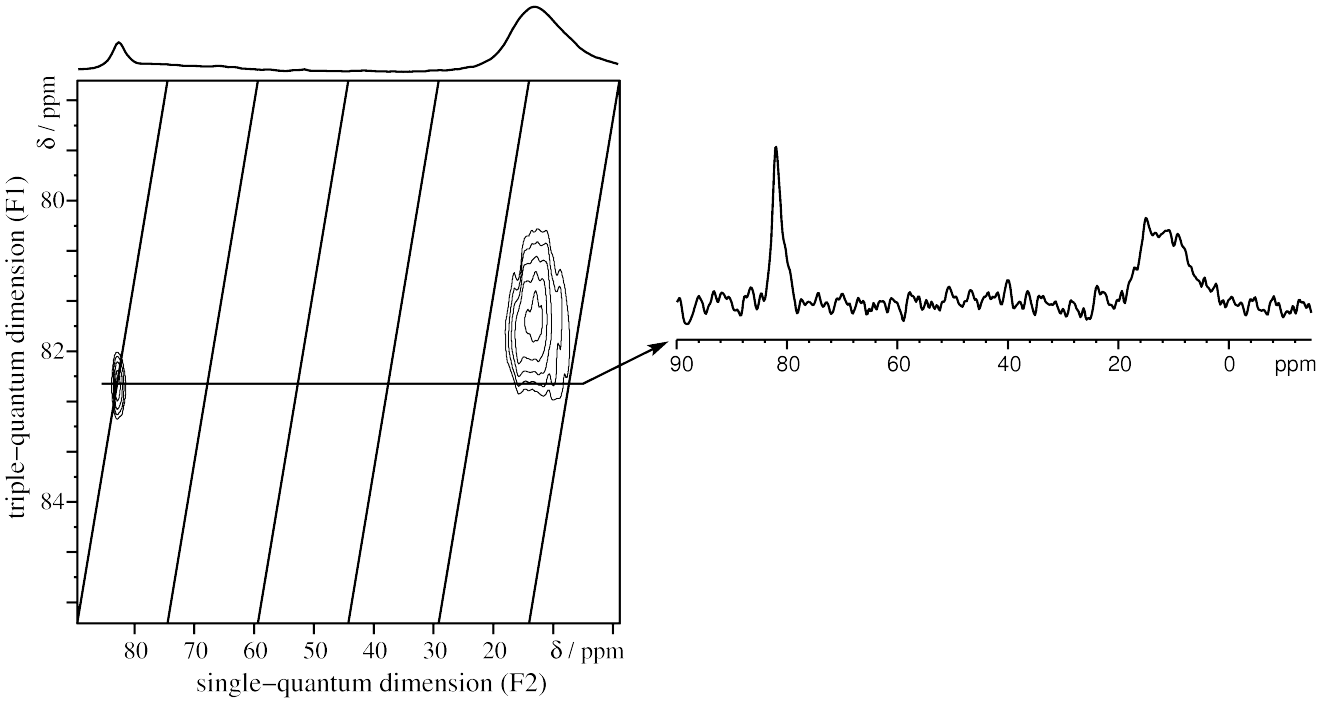

Figure 5: Sheared ^{27}Al 2D MQMAS NMR spectrum with ^{1}H decoupling of as-prepared aluminium-doped zinc oxide (AZO-ap, 1.8 mol %), at a sample spinning frequency of 12 kHz.

^{27}Al MAS NMR peaks are affected by the second-order quadrupolar interaction which can cause a significant broadening even for highly ordered environment in a crystal structure. To distinguish cases of second-order quadrupolar broadening from broadening related to a distribution of environments occurring in amorphous or disordered materials, the multiple-quantum magic angle spinning experiment (MQMAS) was performed. Figure 5 displays a triple-quantum filtered ^{27}Al 2D MQMAS spectrum of AZO-ap. We note that no more than the previously identified Al environments can be resolved in the ^{27}Al MQMAS spectrum.

We now focus on the Al_{Zn} environment ($Al_A^{(IV)}$ -^{27}Al peak) which is related to the metallic properties of the AZO nanoparticles as discussed above. To further characterize this Al environment we have performed a spectral editing experiment on the basis of the different spin-lattice relaxation times T_1 of the different peaks. For the sample AZO-ap we obtained two spectra: spectrum A, with a very long repetition delay τ_{RD} which guarantees complete relaxation of all ^{27}Al peaks and spectrum B, with a repetition delay which guarantees complete relaxation of all peaks except for the fourfold-coordinated aluminium environment $Al_A^{(IV)}$ at 82.6 ppm. The difference spectrum A-B is shown in Figure 4 (d). For

peak $Al_A^{(IV)}$ we additionally obtain an upper limit for the absolute value of the second-order quadrupolar effect parameter *SOQE* of 1.1 MHz from the ^{27}Al MQMAS spectrum (see equation 3), and an isotropic chemical shift of 82.5 ppm, which are consistent with all the observed 1D and 2D ^{27}Al spectra.[44] The *SOQE* is a measure for the quadrupole interaction and can be compared with values predicted by quantum chemical calculations (see below).

^{1}H and ^{13}C NMR - Diethylene Glycol (DEG): The peaks at 3.6 and 4.5 ppm in the ^{1}H MAS NMR spectrum (see SI) are assigned to the methylene and the OH group of DEG. The peak at 1.2 ppm is assigned to the acetic acid or acetate. According to literature,[49] the peaks observed at 71.8 and 61.4 ppm in the ^{13}C{^{1}H} CPMAS spectrum (see SI) can be assigned to the DEG. In addition, there are two extra peaks at 180.2 ppm and 20.9 ppm, which belong to the carboxyl carbon and the methyl carbon of acetic acid or acetate.[88] Thus, the presence of DEG and of acetate groups in the AZO-ap is confirmed by ^{1}H and ^{13}C MAS NMR.

Metallic properties by ^{27}Al relaxation: Relaxation of NMR nuclei in metals shows a temperature dependence with a constant product of spin-lattice relaxation time T_1 and temperature T, (Heitler-Teller or Korringa product89,90) which may be considered as NMR-evidence for metallic properties, next to the above mentioned Knight-shift.

Accordingly, we have performed temperature-dependent relaxation measurements (Figure 6) to provide independent evidence for our ^{27}Al peak assignment, namely that only the peak at 165 ppm in AZO-red stems from a metallic environment, which was found to have similiar T_1 values of around 0.75 s for all three reduced samples (1, 1.8, and 4.6 mol-%). For a simple metallic behavior the Heitler-Teller product is required to be constant, which clearly is only the case for the peak at 165 ppm of the AZO material subject to a reductive treatment (AZO-red 4.6 %), while the curves for the other presented peaks do show a temperature dependence, which is typical for relaxation in ordinary dielectric materials. We conclude that ^{27}Al relaxation measurements confirm the assignment and indicate that only the reduced sample is partially metallic, while the other samples show no evidence for metallic properties.

The Korringa-relation describes how the Heitler-Teller product $T_1 \cdot T$ depends on isotropic Knight-shift *K,*91

$$T_1 T = \frac{\hbar}{4\pi k_B K^2}\left(\frac{\gamma_e}{\gamma_n}\right)^2 \qquad (5)$$

where γ_e and γ_n are the electron and nuclear gyromagnetic ratios, respectively. In a case of the reduced sample (AZO-red, 4.6 %), the experimentally obtained Korringa constant $K^2 T_1 T$ at $T = 220\,\mathrm{K}$ is $3.96 \pm 1.5 \times 10^{-6}$ Ks which agrees well with the theoretical value of 3.87×10^{-6} Ks for non-interacting electrons in the electron gas.

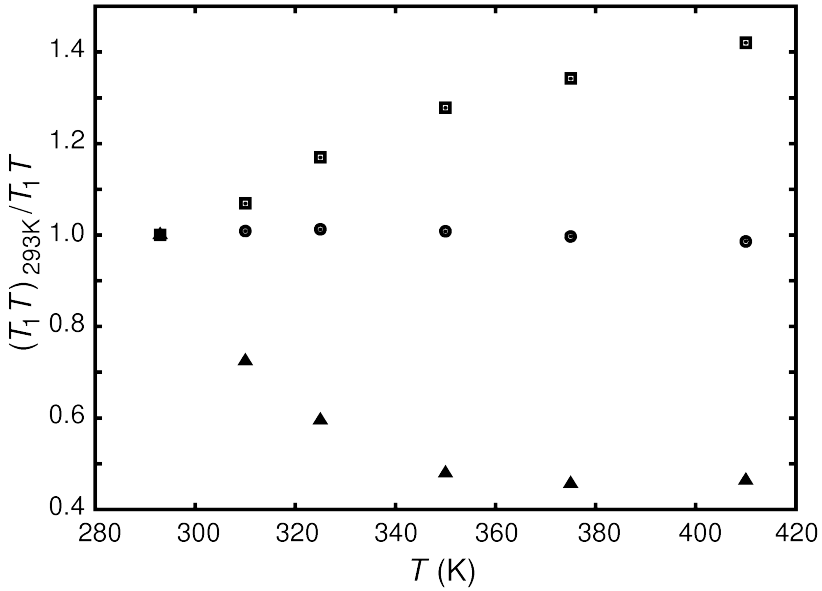

Figure 6: Plot of $1/(T_1 T)$ versus T normalized at 293 K for ^{27}Al NMR peaks of aluminium doped zinc oxide (AZO-red, 4.6 %); circles denote the (approximately constant) Heitler-Teller product for the Knight shifted peak, as expected for a metallic behavior; data denoted by triangles and squares correspond to $Al_B^{(IV)}$ and $Al^{(VI)}$ signals, respectively, diverting from a constant Heitler-Teller product.

Localizing hydrogen in the nanoparticle - ^{27}Al-^{1}H correlated NMR: An interesting question is whether hydrogen occurs only in the particle shell, side-phases or the particle core. The heteronuclear dipolar interaction between ^{27}Al and ^{1}H allows us to prove the occurrence of ^{1}H within a few hundred picometer around the ^{27}Al nucleus. So far we have identified Al in the ZnO crystal structure with the signal $Al_A^{(IV)}$ but we don't know whether these Al atoms are accompanied by hydrogen atoms, for example to form a charge neutral point defect by synchronously replacing two Zn^{2+} ions by H^+ and Al^{3+}. Furthermore we have evidence for the presence of a substantial amount of organic molecules in the as-prepared AZO material but we don't know whether this effect is also related to the Al-doping. To answer these questions we have performed two different experiments: 2D ^{27}Al-^{1}H heteronuclear correlation (HETCOR) spectroscopy and a ^{27}Al{^{1}H} REDOR experiment. The first experiment gives evidence for a potential Al environment close to the organic molecules DEG and acetate; the second

experiment is more sensitive to weak dipole-dipole couplings and maybe used to exclude the occurrence of ^{1}H in the environment of ^{27}Al.

In Figure 7 the 2D $^{27}Al\{^{1}H\}$ HETCOR (2D PRESTO-III) spectrum of AZO-ap (1.8 mol %) is shown. The spectrum proves site connectivities between the components $Al_{B}^{(IV)}$, $Al^{(V)}$ and $Al^{(VI)}$ and the ^{1}H NMR signals from DEG and acetic acid/acetate, but does not give any evidence for ^{1}H in the environment of $Al_{A}^{(IV)}$.

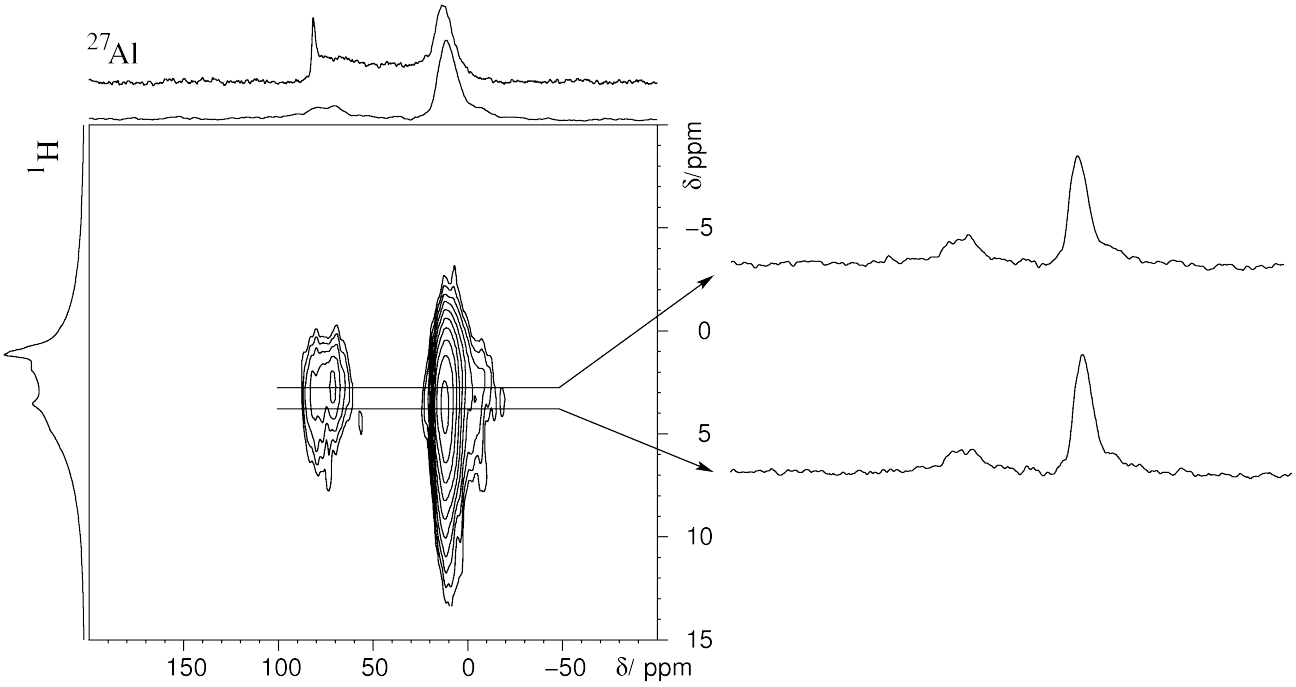

Figure 7: The $^{27}Al\{^{1}H\}$ 2D HETCOR spectrum of the aluminium doped zinc oxide (AZO-ap, 1.8 mol %) nanoparticles, at a field of 11.74 T and a spinning frequency of 10 kHz; spectrum acquired using a ^{1}H-^{27}Al PRESTO-III pulse sequence (Figure 1), using a supercycled $R18_{1}^{7}$ sequence[55] applied to the ^{1}H channel for heteronuclear recoupling; the projections were taken from separate 1D single-pulse excitation experiments; additionally, a sum projection of the 2D PRESTO-III spectrum is shown below the ^{27}Al 1D spectrum at the top of the 2D spectrum.

The findings of the XRD (Figure 3, c) and the 2D $^{27}Al\{^{1}H\}$ heteronuclear correlation spectroscopy also rule out the possibility that the sixfold coordinated aluminium signal $\left(Al^{(VI)}\right)$ comes mainly from a pure, microcrystalline spinel ($ZnAl_2O_4$) phase, as observed on nanoscale AZO materials before.[18,19,24,26] It is possible that the $Al_{B}^{(IV)}$, $Al^{(V)}$ and $Al^{(VI)}$ coordinated Al in the DEG environment are formed as mixed side-phases.

The ^{27}Al{^{1}H} C-REDOR experiment[52] is more sensitive to small dipole-dipole coupling than PRESTO-III. In case of ^{1}H-^{27}Al clusters in the ZnO crystal structure we would expect dephasing of the $Al_A^{(VI)}$ signal. Figure 8 shows C-REDOR curves ($\Delta S = S_0 - S$ as a function of the dephasing time) for $Al_A^{(VI)}$ and $Al^{(VI)}$ in comparison. Within the experimental error the $Al_A^{(VI)}$ peaks are not dephased through heternuclear dipolar coupling of neighboring H atoms, which indicates that the environment of $Al_A^{(VI)}$ is free of hydrogen. The other peaks of $Al_B^{(IV)}$, $Al^{(V)}$ and $Al^{(VI)}$ show a REDOR effect which was expected from the PRESTO-III-experiment (Figure 7) and proves the presence of H atoms in their environment. We conclude that a major part of the doped aluminium is consumed by the shell and side-phase, a fact which might also apply to AZO materials obtained by similar synthetic routes, but which had been neglected so far.[18,19,28]

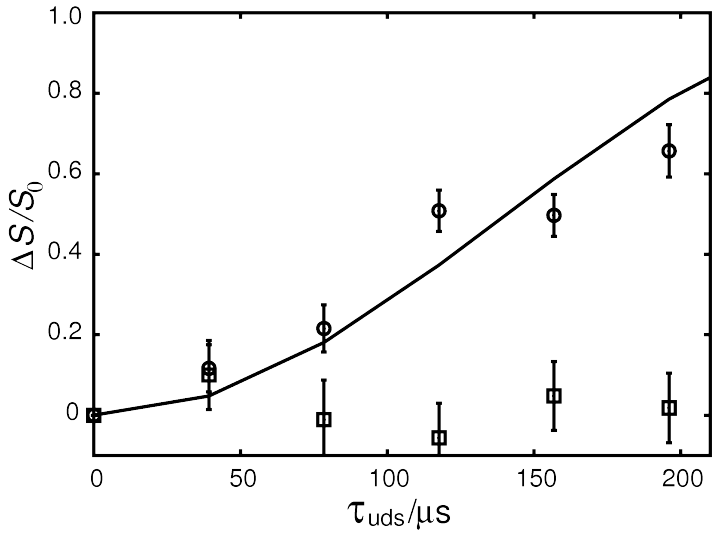

Figure 8: ^{27}Al{^{1}H} NMR C-REDOR curves, ^{27}Al observed, squares and circles with error bars denote experimental data points for the $Al_A^{(IV)}$ and the $Al^{(VI)}$ coordinated sites, respectively; the solid line is a calculated curve for 2 spin-system with a dipole – dipole coupling constant of -2000 Hz; C-REDOR experiment is performed at a magnetic field of 11.74 T.

Effect of increased Al doping concentration on AZO nanoparticles: The AZO nanoparticles are doped with different amounts of aluminium to relate their structure with their electrical properties. Because we have observed a significant amount of Al is in a non-metallic environment, these ^{27}Al NMR signals can be used as a probe to the electrically insulating parts of the material. Clearly the electrical measurements have pointed to an increased sheet resistance at higher doping levels (Table 2). For

homogeneous bulk materials the highest conductivities, i.e. lowest sheet resistivities have been measured at an Al concentration of 1.5wt.%.[21] For heterogeneous materials containing insulating and electrically conductive parts an increased Al content would lead to an increase in the insulating component and therefor to an increase of sheet resistivity.12,92,93

To test this hypothesis we have performed a (semi)-quantitative analysis by ^{27}Al MAS NMR. With an increasing doping percentage of aluminium (1.0, 1.8, and 4.9 mol-%), there are no significant changes in the crystalline component $Al_A^{(IV)}$ of AZO nanoparticles. In Figure 9 (left), the intensity of the crystalline part $Al_A^{(IV)}$ shows no changes for AZO-ap and Figure 9 (right) confirms it with the same intensity of the Knight shifted peak (around 165 ppm) for AZO-red. In contrast to the crystalline component, the intensity of all amorphous aluminium components increases with increasing doping concentrations as shown in Figure 9 (left and right) in AZO-ap as well as AZO-red. This implies that only a limited amount of aluminium is integrated into the crystalline core of the ZnO lattice during synthesis. The remaining aluminium is simply added to the amorphous components/part or side-phases.

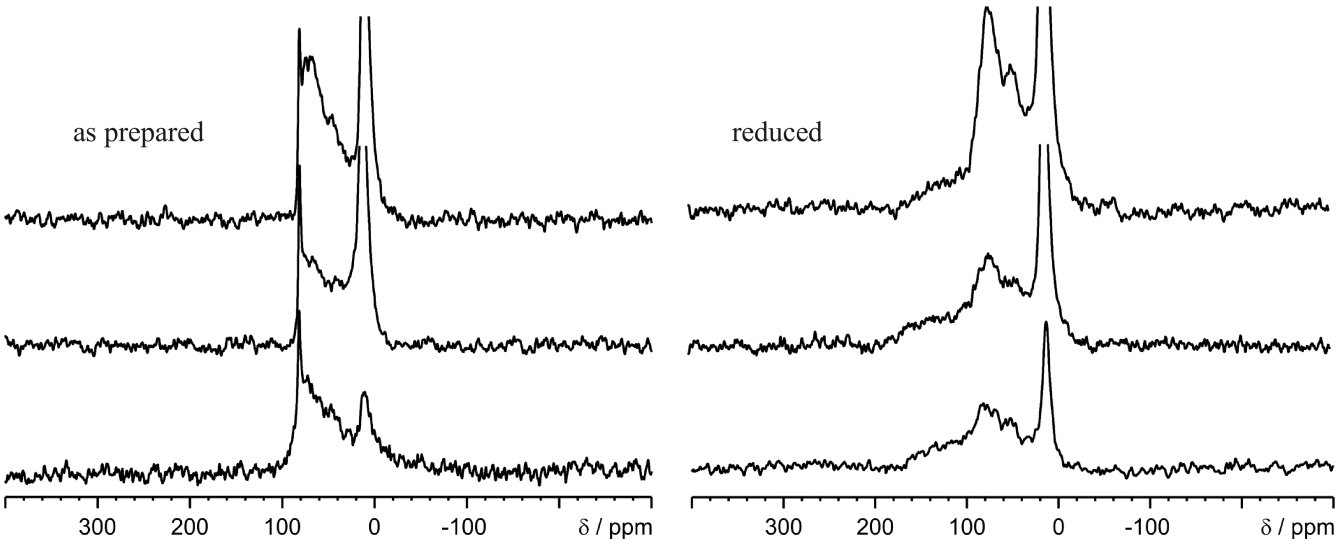

Figure 9: Quantitative 1D ^{27}Al spin echo MAS NMR spectra of aluminium doped ZnO with increasing Al:Zn molar ratio of 1, 1.8, and 4.6 mol-% (bottom to top); (left) AZO-ap nanoparticles (right) AZO-red nanoparticles; performed at 11.74 T, with a spinning frequency of 10 kHz; with approximately same amount of samples packed in the rotor and same experimental conditions; all spectra are plotted approximately on the same y-scale.

More reliable than the visual inspection of the ^{27}Al MAS NMR (Figure 9) is a semi-quantitative

analysis based on ^{27}Al spin-echoes with pulses selective to the central transition. For each identified signal we performed on-resonance excitation separately which means that four spin-echo experiments were performed per sample. The deconvoluted peak areas are displayed in form of a histogram in Figure 10. The histogram shows a nearly constant amount of Al/Zn molar ratio ≈0.12 % for the $Al_A^{(IV)}$ component which is the one we make responsible for the metallic character after reduction. The remaining amorphous components ($Al_B^{(IV)}$, $Al^{(V)}$ and $Al^{(VI)}$) show increasing amount of Al/Zn molar ratio, with increasing aluminium doping concentrations.

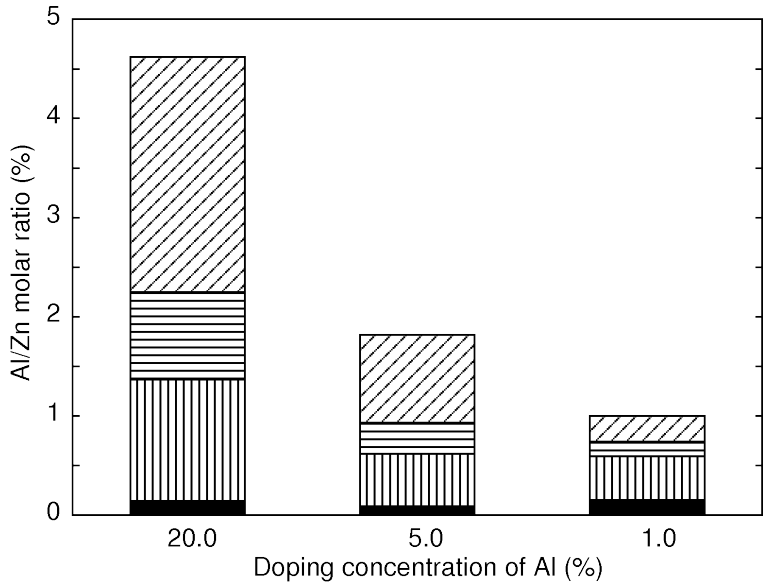

Figure 10: Distribution of Al onto different Al environments in AZO-ap samples with formal doping concentrations of 20%, 5% and 1% in the starting materials corresponding to 4.6%, 1.8% und 1.0% in the product; the measured Al/Zn molar ratio is indicated on the ordinate and splits up into different contributions (from bottom to top): $Al_A^{(IV)}$ (filled black), $Al_B^{(IV)}$ (vertically striped), $Al^{(V)}$ (horizontally striped) and $Al^{(VI)}$ (diagonally striped); the values were estimated by semi-quantitative ^{27}Al spin echo MAS NMR with external referencing at a sample spinning speed of 10 kHz recorded at a magnetic field of 11.74 T; the total amount of Al is in good agreement with the value determined from wet-chemical analysis.

Results from quantum chemical calculations. The target of the quantum chemical calculations was to provide the NMR properties of various doping-induced defects in AZO. To this end we calculated relaxed structures of the defects Al_{Zn}, $Al_{i,Td}$, $Al_{i,Oh}$, $[Al_2V_{Zn}]$, $[Al_{i,Td}V_{Zn}]$ and $[Al_{i,Oh}V_{Zn}]$ in a supercell

approach. The Al concentration in the simulation approaches experimental values because a single Al-atom in a supercell of 36 Zn and O atoms means a dopage of about 2.8% in Al/Zn-ratio.

Technically, we checked whether our calculations are converged with respect to the restricted cell size, by comparing the results of a series of partial structure optimizations taking place in differently sized coordination spheres around the defect. For the following discussion we focus on the results from optimizations up to the second coordination sphere for Al_{Zn}, $Al_{i,Td}$, $Al_{i,Oh}$ and up to the first coordination sphere for the more extended defects $[Al_2V_{Zn}]$, $[Al_{i,Td}V_{Zn}]$ and $[Al_{i,Oh}V_{Zn}]$. In case of Al_{Zn} this turned out to account for the total relaxation almost quantitatively. For the other defects the provided results are probably of more qualitative nature, but should give useful estimates of the relaxed defects, at least. The relaxed structures are shown in Figure 12. Selected structural parameters are given in Table 4 and discussed defect-wise together with the results for the quadrupolar and the chemical shift tensor.

Table 4: Characterization of optimized defect structures. Cols. 2 gives the optimized fraction of the supercell, col. 3 its space group symmetry and col. 4. the stabilization energy (relative to the corresponding unrelaxed structure). Cols. 5-8 denote the four shortest Al-O bond lengths.

defect	optimized part	sym.	$\frac{\Delta E_{relax-unrelax}}{eV}$	$\frac{d(Al-O_i)}{Å}$	$\frac{d(Al-O_j)}{Å}$	$\frac{d(Al-O_k)}{Å}$	$\frac{d(Al-O_m)}{Å}$
$Al_{Zn}^{(0)}$	$Al_{Zn}O_4Zn_{12}$	$P1$	-1.228	1.798	1.800	1.800	1.801
$Al_{i,Oh}^{(0)}$	$Al_{i,Oh}O_4Zn_4$	$P3m1$	-4.152	1.815	1.815	1.815	2.684
$Al_{i,Td}^{(0)}$	$Al_{i,Td}O_4Zn_4$	$P3m1$	-16.606	1.643	1.860	1.860	1.860
$[Al_2V_{Zn}]i^{(0)}$	Al_2O_{10}	$P1$	-2.864	1.783	1.798	1.801	1.814
$[Al_2V_{Zn}]ii^{(0)}$	Al_2O_{10}	$P1$	-2.802[b]	Al_{eq}: 1.758 Al_{ax}: 1.725	1.786 1.779	1.798 1.824	1.857 1.893
$[Al_2V_{Zn}]iii^{(0)}$	Al_2O_{10}	$P1$	-2.719[c]	1.785	1.801	1.812	1.818

[a] relative energy $\{E_{relaxed}(Al_{i,Oh}^{(0)}) - E_{relaxed}(Al_{i,Td}^{(0)})\}$ = -2.183 eV

[b] relative energy $\{E_{relaxed}([Al_2V_{Zn}]i^{(0)}) - E_{relaxed}([Al_2V_{Zn}]ii^{(0)})\}$ = -0.091 eV

[c] relative energy $\{E_{relaxed}([Al_2V_{Zn}]i^{(0)}) - E_{relaxed}([Al_2V_{Zn}]iii^{(0)})\}$ = -0.279 eV

The Al_{Zn} defect. Relaxation of the $Al_{Zn}^{(0)}$ defect leads to a significant stabilization of -1.228 eV (= -118.5 kJ/mol) compared to the non-relaxed defect (see Table 4). The most striking structural changes occur in the first coordination sphere, where a significant decrease of all four Al-O bond distances by 0.16 Å to 0.19 Å is observed (Figure 12a). This is reasonable as Al^{3+} has a smaller ionic radius (0.53 Å)

than Zn^{2+} (0.74 Å),[94] its valence atomic orbitals are more compact and the Al-O bond strength (511 kJ/mol) is substantially larger than the Zn-O bond (159 kJ/mol).[95] In contrast to a previous theoretical study,[31] no significantly distorted structure is found. Instead, we find a local C_3 pseudo-pointgroup symmetry of the $Al_{Zn}O_4$ unit with the rotation axis along the crystal *c*-axis. The calculated displacements from C_3 symmetry are very small (≤0.004 Å) and lead to an energetic stabilization of only -10 J/mol relative to the strictly C_3-symmetric structure (spacegroup $P3m1$ enforced during optimization), which may be attributed to numerical inaccuracies. On the other hand, if the displacement is real, we have a Jahn-Teller-distortion into a very shallow minimum, whose symmetry-equivalent counterparts should be thermally accessible as well, so that C_3-symmetry would be reestablished on the NMR time scale. The structural results for Al_{Zn} hardly change, when an additional electron is removed or added to the supercell (see SI). Moreover, the $Al_{Zn}O_4$ unit is significantly closer to T_d symmetry than a ZnO_4 unit of undoped ZnO. From that we expect a rather small ^{27}Al EFG, i.e. a small quadrupolar coupling constant C_q and an η_q close to zero. Indeed, the EEIM calculations show a C_q of -1.6 MHz and $\eta_q = 0.004$, which explains the small line width of signal $Al_A^{(IV)}$ in Figure 4d. The calculated isotropic chemical shift δ_{iso} of -76.7 ppm is also in fair agreement with the experimental data.† The results disprove a larger distortion of $Al_{Zn}O_4$ from T_d symmetry, as was assumed from analogy to Ga_{Zn} in ZnO.[28] In contrast to Al^{3+} the Ga^{3+} ionic radius is significantly larger, however. The smaller atomic radius for Al and the significant shrinking of the AlO_4 tetrahedron suggests, that the cell parameters of ZnO bulk shrink upon Al_{Zn} dopage. While we did not observe significant changes of cell parameters in our XRD measurements, a shrinking (along the *c* axis) has been reported for AZO-films prepared by magnetron sputtering.[96] It is worth to mention that the structural relaxation is essential to obtain reliable NMR parameters (see Table 5).

† In contrast to previous EEIM calculations, this result is quite sensitive to amount of electrons in the QC. Variations of ±0.5 MHz for C_q and +/-3.3 ppm for δ_{iso} are obtained between the positively and the negatively charged QC. A look at the electron density difference map of the two QCs shows why that is the case: The additional electrons are primarily located at the Zn-atoms next to the AlO_4 unit, where they have a large effect on the calculated properties. In a larger QC or in a more balanced atomic basis set the electrons would probably be more delocalized.

The $Al_{i,Td}$ and the $Al_{i,Oh}$ interstitial sites. The point defects $Al_{i,Td}$ and $Al_{i,Oh}$ have been proposed and named according to the idealized symmetry of the voids in the anionic grid being filled (see Table 1), however the label T_d and *Oh* do not refer to the point group symmetry of the respective Al atom. Upon relaxation of $Al_{i,Td}O_4Zn_4$, i.e. the Al position together with its 8 nearest neighbors† in a $[AlZn_{36}O_{36}]^0$ supercell, the structure is considerably stabilized (see Table 4). Still, the shortest Al-Zn distances (2.029 Å, 2.434 Å, 2.434 Å, 2.434 Å) are short compared to those in $ZnAl_2O_4$, so that the defect is probably too strained to exist in this form. The calculated NMR parameters (see Table 5) of C_q = -19 MHz and δ_{iso} = 104 ppm are not in agreement with any of the experimentally observed signals in Figure 4.

Similar results are obtained for the $Al_{i,Oh}$ site, which – by definition – is located in the channels of the wurtzite structure that are visible when the structure is viewed along the crystal *c*-axis (see Figure 12c). Initially, the Al-atom was placed in the center of an octahedron of six O-atoms with an $Al_{i,Oh}$-O distance of 2.283 Å. Although the total energy per $[Al_{i,Oh}Zn_{36}O_{36}]^0$ supercell is -14.637 eV (=-1412.2 kJ/mol) more stable than the (unrelaxed) $Al_{i,Td}^{(0)}$ site and the relaxation of the $Al_{i,Oh}$ position together with the 12 nearest neighbors mentioned above‡ gives further stabilization by -4.152 eV the structure seems still too strained in view of Al-Zn distances of 2.468 Å and 2.525 Å, respectively. The calculated C_q = -5.76 MHz and δ_{iso} = 93 ppm do not fit to any of the observed NMR signals.

The combined defects $[Al_{i,Td}V_{Zn}]$ and $[Al_{i,Oh}V_{Zn}]$. Because the $Al_{i,Td}$ and $Al_{i,Oh}$ are probably non-existent due to electrostatic repulsion, one might think of interstitial sites next to Zn vacancies, in which the repulsion is reduced. Hence, we created combined defects $[Al_{i,Td}V_{Zn}]^0$ and $[Al_{i,Oh}V_{Zn}]^0$ consisting of an $Al_{i,Td}$ or $Al_{i,Oh}$-interstitial in direct neighborhood to a V_{Zn} defect. Both defects turned out to be unstable and relaxed to the Al_{Zn} defect.

$[Al_2V_{Zn}]$ defects. The $[Al_2V_{Zn}]$ defect consists of two neighboring Al_{Zn} sites and a V_{Zn} void all linked to a central O-site.26 Since the ligands of O in undoped ZnO form an imperfect tetrahedron with C_{3v} symmetry (the atomic distance to the ligand aligned along the crystal *c*-axis is shorter), there are three configurations in which the defect may occur (see Figure 11).

† These neighbors may be shortly termed 1st and 2nd coordination sphere of $Al_{i,Td}$.

‡ These neighbors may be shortly termed 1st and 2nd coordination sphere of $Al_{i,Oh}$.

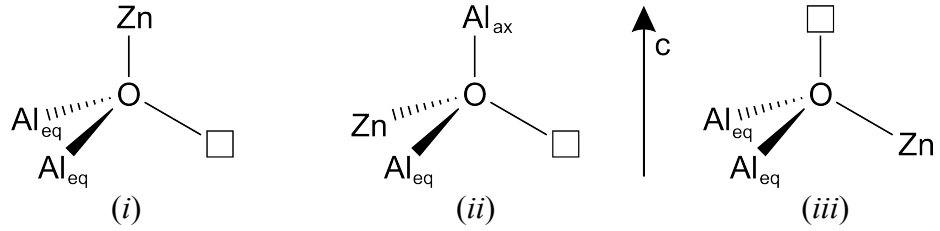

(*i*) (*ii*) (*iii*)

Figure 11: Three possible configurations of the (unrelaxed) [Al_2V_{Zn}] defect. The empty squares denote a vacancy. Indices ax (for axial) and eq (equatorial) refer to the orientation relative to the *c*-axis. Configuration (*ii*) can be realized in two enantiomorphs, which possess the same ^{27}Al NMR properties, however.

All three possibilities were subject to a partial structure optimization including the central oxygen, the Al-sites and the O-sites in the first coordination sphere around Al and the vacancy. All results shown in this section were calculated with a formal doping of two uncharged Al^0, (or $Al_{Zn}^{\bullet} + 1e^-$). The optimized structures are shown in Figure 11(d-e), respectively. Relative energies and a few structural parameters of the [Al_2V_{Zn}] defects are summarized in Table 4. The relaxed [Al_2V_{Zn}]*i* defect is the most stable one, the relaxed [Al_2V_{Zn}]*ii* and [Al_2V_{Zn}]*iii* defects are less stable by 0.091 eV(=8.8 kJ/mol) and 0.279 eV(=26.9 kJ/mol), respectively. The structural relaxation can be understood qualitatively from an electrostatic viewpoint, if the crystal is thought to be composed of positively charged Al and Zn atoms and negatively charged O atoms, as well as from a bond theoretical viewpoint. The oxygen ligands around the Al move towards the Al-sites, because Al has a higher core charge (Al^{3+}) and more compact valence orbitals than Zn. The oxygen neighbors next to the void lack an attractive force in the direction of the void, hence they move away from it. The central oxygen atom of the [Al_2V_{Zn}] defect shown in Figure 11 experiences both effects simultaneously and shows therefor the largest relaxation displacement.

The calculated NMR parameters C_q and δ_{iso} of the [Al_2V_{Zn}] defects lie in the range of the experimental signal $Al_B^{(IV)}$. However, as the ^{27}Al{^{1}H} HETCOR and C-REDOR measurements (Figure 7 and 8) indicate, there is hydrogen present nearby $Al_B^{(IV)}$, but not $Al_A^{(IV)}$. This rules out an assignment of $Al_B^{(IV)}$ to [Al_2V_{Zn}] defects in ZnO bulk.

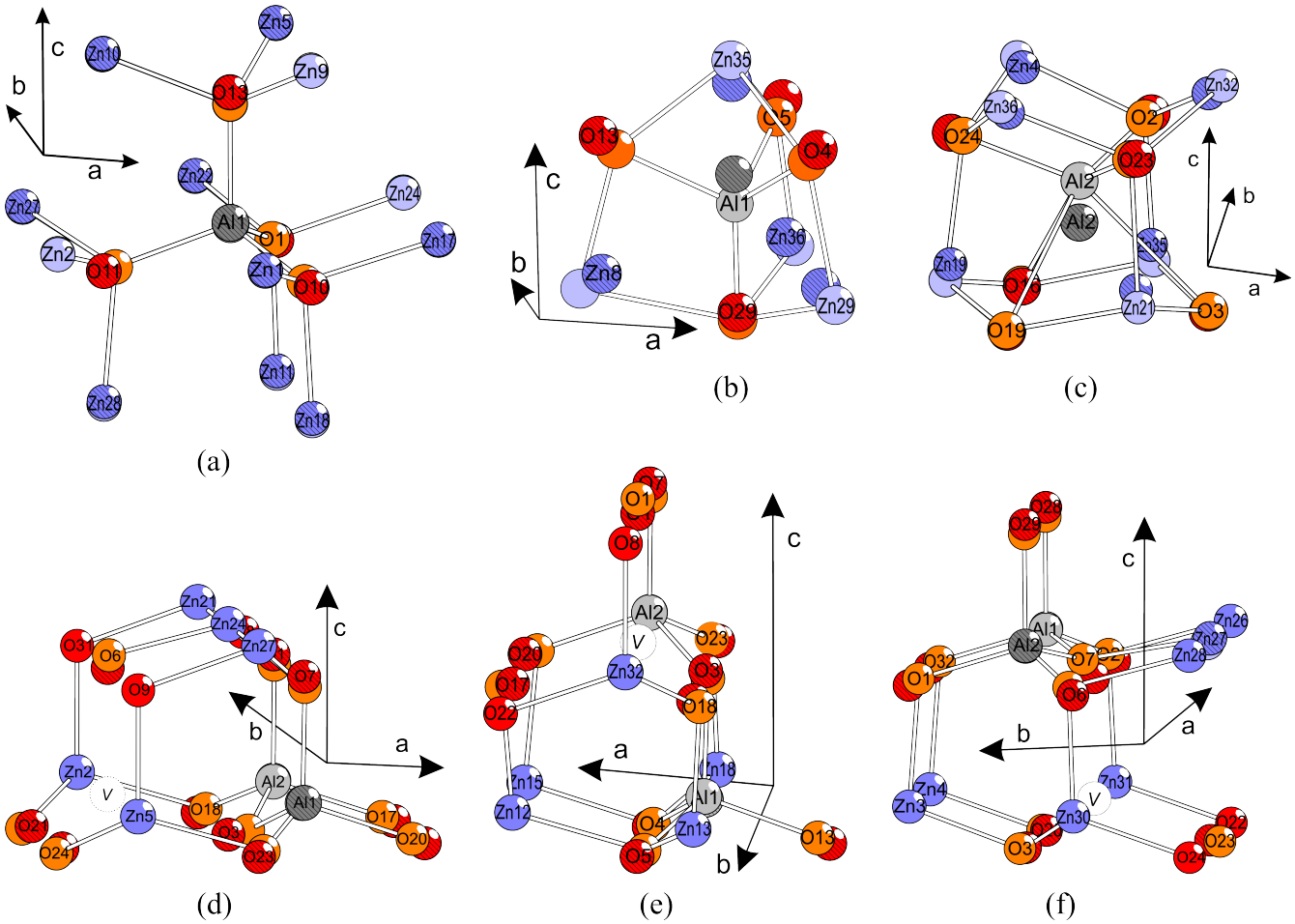

Figure 12: Comparison of non-optimized and relaxed structures of various defect sites in ZnO:Al. (a) Al_{Zn}, (b) $Al_{i,Td}$, (c) $Al_{i,Oh}$-, (d) $[Al_2V_{Zn}]$, config. *i*), (e) $[Al_2V_{Zn}]$, config. *ii*), (f) $[Al_2V_{Zn}]$, config. *iii*). Oxygen sites are drawn in orange if relaxed or red if unrelaxed, zinc sites in light blue (relaxed) or blue (unrelaxed), aluminium sites in light grey (relaxed) or grey (unrelaxed). Non-optimized sites corresponding to optimized ones are hatched, voids are indicated by empty circles. Sites belonging to structures (a-c) are optimized up to second coordination sphere with respect to the point defects, structures (d-f) up to first sphere (see text for details).

Table 5: Calculated ^{27}Al nuclear quadrupole coupling constants, anisotropy, second order quadrupolar effects and chemical shift parameters for various kinds of relaxed defects, if not mentioned otherwise.

type of defect		C_q / MHz	ε_q	*SOQE*/ MHz	δ_{iso}/ ppm	Assignment to exp. peak
Al_{Zn}	relaxed	-1.6[a]	0.00	-1.6	76.7[a]	$^{(IV)}Al_A$
(Al_{Zn}	unrelaxed	-2.4	0.07	-2.5	58.4	)
$Al_{i,Td}$		-19.1	0.00	-19.1	103.5	none
$Al_{i,Oh}$		5.8	0.00	5.8	93.4	none
[Al_2V_{Zn}] *i*	$Al1_{eq}$	-4.7	0.65	-5.6	74.6	none
	$Al2_{eq}$	-4.3	0.72	-5.2	74.8	
[Al_2V_{Zn}] *ii*	$Al1_{ax}$	-12.1	0.89	-15.3	74.1	none
	$Al2_{eq}$	9.2	0.96	11.8	75.0	
[Al_2V_{Zn}] *iii*	$Al1_{eq}$	-5.5	0.65	-6.6	74.5	none
	$Al2_{eq}$	-5.5	0.66	-6.6	74.5	

[a] The values are rather sensitive to the number of electrons placed in the QC, and are calculated by averaging over values from $[Zn_{38}O_{39}Al]^+$ and $[Zn_{38}O_{39}Al]^-$ clusters, whose values are C_q=-2.12 and -1.11 MHz or δ_{iso}=80.0 and 73.4 ppm, respectively. This corresponds to a formal doping with $Al_{Zn}^{\bullet} + 1e^-$, where the open shell character of this configuration is avoided, however.

Overall Discussion

The investigations in this work lead to a largely revised picture of Al-doping into ZnO. The defects $Al_{i,Td}$, $Al_{i,Oh}$, [Al_2V_{Zn}] and side-phases of pure, but microcristalline $ZnAl_2O_4$, that were considered as potential candidates in earlier works of nano-wires and bulk AZO, could be ruled out in our sample by NMR measurements and quantum chemical (DFT) calculations.

The structure of the AZO nano-particles can be envisaged as depicted in Figure 13. It consists of particles with a crystalline ZnO core of approximately 8-12 nm in diameter (DLS, XRD, TEM) which is the only crystalline phase we observed by X-ray diffraction. The core contains a small amount of Al doping which we identified by ^{27}Al NMR and DFT. It occupies a highly ordered fourfold O-coordinated Al $\left(Al_A^{(IV)}\right)$ environment. The shell or side-phase contains Al and the organic molecules. The aluminium environments such as $Al_B^{(IV)}$, $Al^{(V)}$ and $Al^{(VI)}$ were identified by ^{27}Al NMR and were shown to contain hydrogen atoms belonging to the organic molecules DEG and acetate (^{27}Al{^{1}H}-REDOR, ^{27}Al{^{1}H}-PRESTO-III). From the facts that no unidentified reflexes are observed in the XRD pattern and that the ^{27}Al NMR signals are relatively broad, we infer that the shell or side-phases are

highly disordered.

The different, initially synthesized nanoparticles (AZO-ap/-ox) macroscopically behave as insulators. By ^{27}Al-NMR we observe only ^{27}Al resonances typical for insulating materials, indicating that the electrons added through Al-doping are trapped for example in form of OH-functions and localized at the particle surface. Thus we do not have any evidence for the case of metallic particles in an insulating shell which would also possess a high-sheet resistivity.

After the reductive treatment (AZO-red) the particles show metallic behavior both macroscopically as evidenced by the conductivity measurements and microscopically as evidenced by the occurrence of a Knight-shifted ^{27}Al peak with a Korringa-type relaxation behavior.

This interpretation is underlined by a concentration series in which the Al doping concentration was varied. Macroscopically the sheet resistivity has its minimum around 1% Al/Zn ratio. While small amounts of Al are beneficial to the electron concentration in the ZnO conduction band (n-doping), the Al equilibrium concentration under the chosen chemical conditions in ZnO is so small that the excess of Al is consumed by insulating side-phases and the shell as evidenced by ^{27}Al-NMR, which causes a tremendous increase in sheet resistivity.

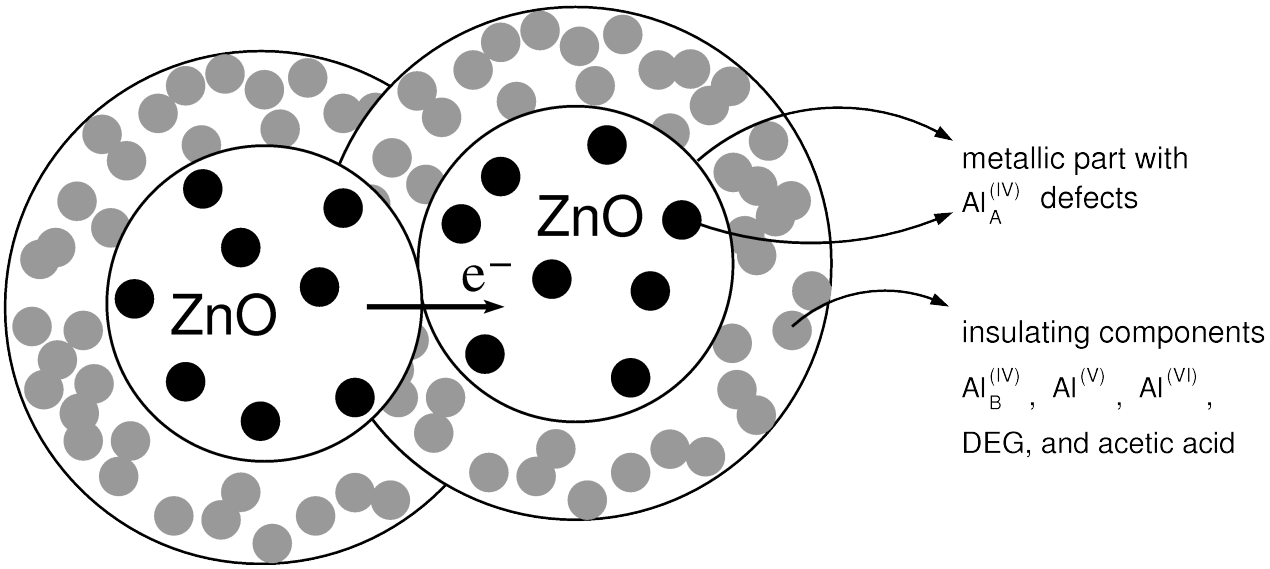

Figure 13: Model of a polycrystalline AZO-red nanoparticles; within the metallic ZnO crystallites the dopant Al fills individual Zn vacancies Al_{Zn} (i.e. $Al_A^{(IV)}$); the ZnO nanoparticles are covered by non-conductive heavily disordered phases which contain four- $\left(Al_B^{(IV)}\right)$, five- $\left(Al^{(V)}\right)$ and sixfold-coordinated $\left(Al^{(VI)}\right)$ aluminium components and diethylene glycole (DEG) and acetic acid/acetate.

Conclusions

A model of the core-shell structure of aluminium-doped zinc oxide nanoparticles has been derived. The model has been verified on particles synthesized from a microwave-assisted polyol method. We have shown that a combination of different 1D ^{27}Al, ^{1}H, ^{13}C and 2D $^{27}Al\{^{1}H\}$ solid-state NMR techniques provides detailed insight into the particle structure and allows to explain the macroscopically observed conductivities as a function of the particle composition. We have identified a fourfold-coordinated Al environment as the only one being relevant for the improved electrical conductivity. Moreover we have found that any Al above a certain threshold, that is added to the start mixture, is consumed by an electrically insulating side-phase or shell, which is counterproductive with respect to achieving high macroscopic conductivity. We conclude that solid-state NMR offers excellent tools to investigate the interior of nanoparticles which may help to guide the synthesis of nanoscale TCOs but also nanoscale materials in general. Beside the material aspects of this contribution we have implemented a 2D correlation NMR experiment based on the PRESTO-III experiment.

Acknowledgment

E. H. and C. F. are grateful to W. Send and Prof. Dr. D. Gerthsen for performing TEM analysis. We also acknowledge the DFG Center for Functional Nanostructures (CFN) at the Karlsruhe Institute of Technology (KIT) for financial support. J. S. a. d. G., J. W. and Y. S. A. gratefully acknowledge financial support through the Emmy-Noether program of the DFG (SCHM1570-2/1), Munich University (LMU). We also thank to C. Minke for technical support. We are also grateful to Prof. Dr. W. Schnick for the possibility to use the facilities at the chair of inorganic solid-state chemistry. J. W. thanks the Leibnitz-Rechenzentrum in Garching for computational facilities.

Supporting Information: Details of the quantum chemical calculations, SEM images of as-prepared AZO-ap (1.0, 1.8 and 4.9 mol %), ^{1}H MAS NMR and ^{13}C{^{1}H} CPMAS NMR spectrum. ^{27}Al{^{1}H} 2D HETCOR of oxidized and reduced AZO (1.8 mol %).

References

1. K. L. Chopra, S. Major, and D. K. Pandya, *Thin Solid Films*, 1983, **102**, 1-46.
2. T. Minami, H. Nanto, and S. Takata, *Jpn. J. Appl. Phys.*, 1984, **23**, L280-L282.
3. K. Ellmer, A. Klein, and B. Rech, *Transparent Conductive Zinc Oxide*, Berlin, 2008, vol. 104.
4. U. Özgür, Y. I. Alivov, C. Liu, A. Teke, M. A. Reshchikov, S. Doğan, V. Avrutin, S.-J. Cho, and H. Morkoç, *J. Appl. Phys.*, 2005, **98**, 041301.
5. T. D. Kelly and G. R. Matos, in *Historical statistics for mineral and material commodities in the United States*, 2011.
6. C. G. Granqvist, *Sol. Energy Mater. Sol. Cells*, 2007, **91**, 1529-1598.
7. H. Sato, T. Minami, T. Miyata, S. Takata, and M. Ishii, *Thin Solid Films*, 1994, **246**, 65-70.
8. J. G. Lu, S. Fujita, T. Kawaharamura, H. Nishinaka, Y. Kamada, T. Ohshima, Z. Z. Ye, Y. J. Zeng, Y. Z. Zhang, L. P. Zhu, H. P. He, and B. H. Zhao, *J. Appl. Phys.*, 2007, **101**, 083705.
9. J. U. Brehm, M. Winterer, and H. Hahn, *J. Appl. Phys.*, 2006, **100**, 064311.
10. M. Hilgendorff, L. Spanhel, C. Rothenhausler, and G. Muller, *J. Electrochem. Soc.*, 1998, **145**, 3632-3637.
11. T. Schuler and M. A. Aegerter, *Thin Solid Films*, 1999, **351**, 125-131.
12. J.-H. Lee and B.-O. Park, *Thin Solid Films*, 2003, **426**, 94-99.
13. V. Musat, B. Teixeira, E. Fortunato, R. C. C. Monteiro, and P. Vilarinho, *Surf. Coat. Technol.*, 2004, **180-181**, 659-662.
14. M. Niederberger, *Acc. Chem. Res.*, 2007, **40**, 793-800.
15. Y. Zhang, Y. Yang, J. Zhao, R. Tan, W. Wang, P. Cui, and W. Song, *J. Mater. Sci.*, 2011, **46**, 774-780.
16. K. J. Chen, T. H. Fang, F. Y. Hung, L. W. Ji, S. J. Chang, S. J. Young, and Y. J. Hsiao, *Appl.*

Surf. Sci., 2008, **254**, 5791-5795.
17. S. Hartner, M. Ali, C. Schulz, M. Winterer, and H. Wiggers, *Nanotechnology*, 2009, **20**, 445701.
18. R. Noriega, J. Rivnay, L. Goris, D. Kälblein, H. Klauk, K. Kern, L. M. Thompson, A. C. Palke, J. F. Stebbins, J. R. Jokisaari, G. Kusinski, and A. Salleo, *J. Appl. Phys.*, 2010, **107**, 074312.
19. T. Kemmitt, B. Ingham, and R. Linklater, *J. Phys. Chem. C*, 2011, **115**, 15031-15039.
20. H. Wang, M. H. Xu, J.-W. Xu, M.-fang Ren, and L. Yang, *J. Mater. Sci. - Mater. Electron.*, 2009, **21**, 589-594.
21. B. Szyszka, *Thin Solid Films*, 1999, **351**, 164-169.
22. R. D. J. Tilley, in *Understanding Solids*, Wiley & Sons, Chichester, 2004, pp. 73-84.
23. F. Oba, H. Ohta, Y. Sato, H. Hosono, T. Yamamoto, and Y. Ikuhara, *Phys. Rev. B*, 2004, **70**, 125415.
24. R. Noriega, L. Goris, J. Rivnay, J. Scholl, L. M. Thompson, A. C. Palke, J. F. Stebbins, and A. Salleo, *Proc. of SPIE*, 2009, **7411**, 74110N-1.
25. L. Goris, R. Noriega, M. Donovan, J. Jokisaari, G. Kusinski, and A. Salleo, *J. Electron. Mater.*, 2008, **38**, 586-595.
26. H. Serier, M. Gaudon, and M. Ménétrier, *Solid State Sci.*, 2009, **11**, 1192-1197.
27. R. Wang, A. W. Sleight, and D. Cleary, *Chem. Mater.*, 2011, **8**, 433-439.
28. N. Roberts, R.-P. Wang, A. W. Sleight, and W. W. Warren, Jr., *Phys. Rev. B*, 1998, **57**, 5734.
29. W. W. Warren, N. Roberts, R. P. Wang, and A. W. Sleight, *Phys. Rev. B*, 1997, **258-263**, 1365-1370.
30. T. Tsubota, M. Ohtaki, K. Eguchi, and H. Arai, *J. Mater. Chem.*, 1997, **7**, 85-90.
31. F. Maldonado and A. Stashans, *J. Phys. Chem. Solids*, 2010, **71**, 784-787.
32. C. G. Van de Walle, *Phys. Status Solidi B*, 2003, **235**, 89-95.
33. C. G. Van de Walle, *Phys. Rev. Lett.*, 2000, **85**, 1012.
34. A. Janotti and C. G. Van de Walle, *physica status solidi (b)*, 2011, **248**, 799-804.
35. A. A. Sokol, S. A. French, S. T. Bromley, C. R. A. Catlow, H. J. J. van Dam, and P. Sherwood, *Faraday Discuss.*, 2006, **134**, 267-282.
36. F. Oba, M. Choi, A. Togo, and I. Tanaka, *Science and Technology of Advanced Materials*, 2011, **12**, 034302.
37. X. M. Duan, C. Stampfl, M. M. M. Bilek, and D. R. McKenzie, *Phys. Rev. B*, 2009, **79**, 235208.
38. W. Körner and C. Elsässer, *Phys. Rev. B*, 2010, **81**, 085324.
39. F. A. Kröger, *The chemistry of imperfect crystals*, North-Holland Pub. Co., 1964.
40. Y.-I. Chen and J.-G. Duh, *Mater. Chem. Phys.*, 1991, **27**, 427-439.
41. E. Hammarberg, A. Prodi-Schwab, and C. Feldmann, *J. Colloid Interface Sci.*, 2009, **334**, 29-36.
42. R. K. Harris, E. D. Becker, S. M. Cabral de Menezes, P. Granger, R. E. Hoffman, and K. W. Zilm, *Pure Appl. Chem.*, 2008, **80**, 59-84.
43. G. Metz, X. L. Wu, and S. O. Smith, *J. Magn. Reson.*, 1994, **110**, 219-227.
44. J.-P. Amoureux, C. Fernandez, and S. Steuernagel, *J. Magn. Reson. A*, 1996, **123**, 116-118.
45. D. States, R. Haberkorn, and D. Ruben, *J. Magn. Reson.*, 1982, **48**, 286-292.
46. B. Herreros, A. W. Metz, and G. S. Harbison, *Solid State Nucl. Magn. Reson.*, 2000, **16**, 141-150.
47. J. C. C. Chan, *Chem. Phys. Lett.*, 2001, **335**, 289-297.
48. J. C. C. Chan and H. Eckert, *J. Chem. Phys.*, 2001, **115**, 6095.

49. M. Roming, C. Feldmann, Y. S. Avadhut, and J. Schmedt auf der Günne, *Chem. Mater.*, 2008, **20**, 5787-5795.
50. Y. S. Avadhut, J. Weber, E. Hammarberg, C. Feldmann, I. Schellenberg, R. Pöttgen, and J. Schmedt auf der Günne, *Chem. Mater.*, 2011, **23**, 1526-1538.
51. A. Brinkmann and M. H. Levitt, *J. Chem. Phys.*, 2001, **115**, 357.
52. T. Gullion and J. Schaefer, *J. Magn. Reson.*, 1989, **81**, 196-200.
53. M. Bak, J. T. Rasmussen, and N. C. Nielsen, *J. Magn. Reson.*, 2000, **147**, 296-330.
54. T. Vosegaard, A. Malmendal, and N. C. Nielsen, *Monatsh. Chem.*, 2002, **133**, 1555-1574.
55. X. Zhao, W. Hoffbauer, J. Schmedt auf der Günne, and M. H. Levitt, *Solid State Nucl. Magn. Reson.*, 2004, **26**, 57-64.
56. G. Kresse and J. Furthmüller, *Phys. Rev. B*, 1996, **54**, 11169-11186.
57. G. Kresse and J. Hafner, *Phys. Rev. B*, 1993, **47**, 558-561.
58. G. Kresse and J. Hafner, *Phys. Rev. B*, 1994, **49**, 14251-14269.
59. G. Kresse and J. Furthmüller, *Comput. Mater. Sci.*, 1996, **6**, 15-50.
60. P. E. Blöchl, *Phys. Rev. B*, 1994, **50**, 17953-17979.
61. G. Kresse and D. Joubert, *Phys. Rev. B*, 1999, **59**, 1758-1775.
62. H. J. Monkhorst and J. D. Pack, *Phys. Rev. B*, 1976, **13**, 5188-5192.
63. J. P. Perdew, A. Ruzsinszky, G. I. Csonka, O. A. Vydrov, G. E. Scuseria, L. A. Constantin, X. Zhou, and K. Burke, *Phys. Rev. Lett.*, 2008, **100**, 136406.
64. Heller, R. B., McGannon, J., and Weber, A.H., *J. Appl. Phys.*, 1950, **21**, 1283-1284.
65. H. A. Jahn and E. Teller, *Proc. R. Soc. London, Ser. A*, 1937, **161**, 220 -235.
66. J. Weber and J. Schmedt auf der Günne, *Phys. Chem. Chem. Phys.*, 2010, **12**, 583–603.
67. D. Stueber, *Concepts Magn. Reson., Part A*, 2006, **28A**, 347-368.
68. D. Stueber, F. N. Guenneau, and D. M. Grant, *J. Chem. Phys.*, 2001, **114**, 9236.
69. Y. S. Avadhut, J. Weber, E. Hammarberg, C. Feldmann, I. Schellenberg, R. Pöttgen, and J. Schmedt auf der Günne, *Chem. Mater.*, 2011, **23**, 1526–1538.
70. P. Schwertfeger, M. Pernpointner, and W. Nazarewicz, in *Calculation of NMR and EPR Parameters. Theory And Applications.*, Wiley-VCH, Weinheim, 2004, pp. 279-291.
71. M. Strohmeier, D. Stueber, and D. M. Grant, *J. Phys. Chem.*, 2003, **A107**, 7629–7642.
72. C. Adamo and V. Barone, *J. Chem. Phys.*, 1998, **108**, 664–675.
73. M. J. Frisch, and *et al.*, *Gaussian 03*, Gaussian Inc., Wallingford, CT, 2004.
74. E. D. Glendering, J. K. Badenhoop, A. E. Reed, J. E. Carpenter, J. A. Bohmann, C. M. Morales, and F. Weinhold, *NBO 5.0*, University of Wisconsin, Theoretical Chemistry Institute, Madison (Wisconsin, US), 2001.
75. A. D. McLean and G. S. Chandler, *J. Chem. Phys.*, 1980, **72**, 5639–5648.
76. M. M. Francl, W. J. Petro, W. J. Hehre, J. S. Binkley, M. S. Gordon, D. J. DeFrees, and J. A. Pople, *J. Chem. Phys.*, 1982, **77**, 3654–3665.
77. W. J. Stevens, M. Krauss, H. Basch, and P. G. Jasien, *Can. J. Chem.*, 1992, **70**, 612.
78. F. Jensen, *J. Chem. Theory Comput.*, 2008, **4**, 719-727.
79. T. Vosegaard, J. Skibsted, H. Bildsoe, and H. J. Jakobsen, *J. Phys. Chem.*, 1995, **99**, 10731-10735.
80. J. Skibsted, N. C. Nielsen, H. Bildsøe, and H. J. Jakobsen, *J. Magn. Reson.*, 1991, **95**, 88-117.

81. P. Pyykkö, *Mol. Phys.*, 2001, **99**, 1617–1629.
82. K. Wolinski, J. F. Hinton, and P. Pulay, *J. Am. Chem. Soc.*, 1990, **112**, 8251–8265.
83. T. Vosegaard and H. J. Jakobsen, *J. Magn. Reson.*, 1997, **128**, 135-137.
84. C. Feldmann, *Adv. Funct. Mater.*, 2003, **13**, 101-107.
85. W. L. Bragg, *Philos. Mag.*, 1920, **39**, 647-651.
86. T. Minami, *Semicond. Sci. Technol.*, 2005, **20**, S35-S44.
87. K. J. D. MacKenzie and M. E. Smith, *Multinuclear Solid-State Nuclear Magnetic Resonance of Inorganic Materials*, Pergamon, 2002.
88. M. Hesse, H. Meier, and B. Zeeh, *Spektroskopische Methoden in der Organischen Chemie*, Thieme Verlag, Stuttgart,Germany, 1991.
89. J. J. van der Klink and H. B. Brom, *Prog. Nucl. Magn. Reson. Spectrosc.*, 2000, **36**, 89-201.
90. J. Korringa, *Physica*, 1950, **16**, 601-610.
91. C. P. Slichter, *Principles of Magnetic Resonance*, Springer-Verlag, Berlin, 1992.
92. M. J. Alam and D. C. Cameron, *J. Vac. Sci. Technol., A*, 2001, **19**, 1642.
93. M. H. Mamat, M. Z. Sahdan, Z. Khusaimi, A. Z. Ahmed, S. Abdullah, and M. Rusop, *Opt. Mater.*, 2010, **32**, 696-699.
94. R. D. Shannon, *Acta Crystallogr., Sect. A*, 1976, **32**, 751-767.
95. D. R. Lide, *CRC Handbook of Chemistry and Physics, CDROM Version*, CRC Press, 2003.
96. K. C. Park, D. Y. Ma, and K. H. Kim, *Thin Solid Films*, 1997, **305**, 201-209.